PAPER

Check for updates

Electrochemical performance and durability of high-temperature solid oxide electrolysis cells with SFM and SFM-GDC fuel electrodes for hydrogen and syngas production

Stephanie E. Wolf, [ab] Vaibhav Vibhu, [*a] Pritam K. Chakraborty, [ab] Carla L. Coll, [a] Sandro Schöner, [ab] Shibabrata Basak, [a] Izaak C. Vinke, [a] L. G. J. (Bert) de Haart [a] and Rüdiger-A. Eichel [ab]

The present study focuses on highly catalytic double-perovskite $Sr_2FeMoO_{6-\delta}$ (SFM) fuel electrode materials for Solid Oxide Electrolysis Cells (SOECs). The redox stability was characterized using XRD and *in situ* TEM analyses to visualize phase conversion above 800 °C after reduction in Ar-3–4% H_2. Phase formation of mixed Ruddlesden–Popper, (double-) perovskite phases, and Fe nanoparticle exsolution was observed and related to the in *operando* enhanced catalytic performance. Electrolyte-supported single cells with SFM (-$Ce_{0.8}Gd_{0.2}O_{1.9}$)/GDC/8YSZ/GDC/$La_{0.58}Sr_{0.4}Co_{0.2}Fe_{0.8}O_3$ (LSCF) were prepared and electrochemically evaluated in the range of 750 °C to 900 °C using DC- and AC-techniques. The high electrochemical performance of −1.26 A cm^{-2} and −1.27 A cm^{-2} under steam and co-electrolysis conditions respectively, exceeded state-of-the-art Ni-YSZ by ∼38% and was comparable to Ni-GDC fuel electrodes in electrolyte-supported button cells. A long-term durability test was conducted for 500 h at −0.3 A cm^{-2} and 900 °C under steam electrolysis conditions with a fuel gas composition of 50% H_2O + 50% H_2. The SFM-GDC fuel electrode showed outstanding stability of 0.016 mV h^{-1} for 500 h measurement. The SFM electrode exhibited a high degradation of around 0.765 mV h^{-1} and a striking structural instability through the evolution of a dense layer at the SFM/GDC interface after 300 h.

1. Introduction

Maritime and aviation industries play a factor in global anthropogenic emissions that include carbon dioxide (CO_2), methane (CH_4), and nitrous oxide (N_2O). Hydrogen (H_2) has emerged as an alternative carbon-neutral and non-toxic fuel that can be produced through the established electrolysis of water (H_2O) from renewably generated power sources such as solar, wind, and hydropower. However, the current hydrogen production mainly focuses on gray power sources such as natural gas reforming.[1] High-temperature electrolysis in a Solid Oxide Electrolysis Cell (SOEC) is a key technology that allows the production of H_2 product gas at elevated operating temperatures between 650 °C to 900 °C without detrimental impurities.[2,3] The stacked cells consist of an oxide ion conducting electrolyte between two porous electrodes. Gaseous H_2O is reduced in an endothermic reaction at the negatively charged fuel electrode to hydrogen and oxygen ions (eqn (1)). The

generated O^{2-} ions migrate through the electrolyte to the positively charged oxygen electrode, where the oxygen evolution reaction (OER) takes place (eqn (4)). SOECs can also electrolyze pure CO_2 (eqn (2)) as well as a gas mixture of CO_2/H_2O (so-called co-electrolysis) to produce synthesis gas, a gaseous product mixture of H_2 and carbon monoxide (CO). Various liquid hydrocarbon-based synthetic fuels, including methanol, and methane can be derived from this synthesis gas, thereby valorizing emitted CO_2 and closing the carbon cycle.[4–7] In high-temperature co-electrolysis, the ratio of the gaseous products H_2 and CO can be tailored to meet the requirements of downstream processes by carefully adjusting the feedstock mixture of CO_2 and H_2O. Depending on the operating conditions, the process equilibrium influences the (reverse) water gas shift reaction ((R)WGS) and thereby the product ratio (eqn (3)).[8,9]

$$2H_2O + 4e^- \rightarrow 2H_2 + 2O^{2-} \quad \Delta H_{800°C} = -247.88 \text{ kJ mol}^{-1} \quad (1)$$

$$2CO_2 + 4e^- \rightarrow 2CO + 2O^{2-} \quad \Delta H_{800°C} = -280.50 \text{ kJ mol}^{-1} \quad (2)$$

$$CO_2 + H_2 \rightleftharpoons CO + H_2O \quad \Delta H_{800°C} = 36.8 \text{ kJ mol}^{-1} \quad (3)$$

$$2O^{2-} \rightarrow 4e^- + O_2 \quad (4)$$

Institute of Energy Technologies, Fundamental Electrochemistry (IET-1), Forschungszentrum Jülich GmbH, 52425, Jülich, Germany. E-mail: v.vibhu@fz-juelich.de; Tel: +49-2461-61-6553

Institute of Physical Chemistry, RWTH Aachen University, 52074 Aachen, Germany

The elevated operating temperatures in the solid oxide electrolyzers have thermodynamic and kinetic advantages compared to other low-temperature (LT) electrolysis technologies, *i.e.*, alkaline electrolysis (AE) and polymer exchange membrane (PEM) cells, which results in exceedingly high electrical efficiencies of up to 100%. In addition, the required process energy can be supplied as heat from pre-existing chemical industry plants.[10,11] The commonly employed catalyst materials in SOEC systems for the hydrogen evolution reaction (HER) are composite materials based on non-expensive Ni, which makes SOEC stacks more cost-effective in comparison to alkaline and PEM electrolyzers. Currently used electrodes for the HER reaction are Ni-YSZ and Ni-GDC cermet electrodes, which are composed of electronic-conducting metallic Ni and the ionic conducting 8 mol% yttria-stabilized ZrO_2 (8YSZ) or gadolinium-stabilized ceria (GDC).

Despite the high performance of Ni cermet electrodes, high-temperature electrolysis necessitates thermostable materials for long-term hydrogen and synthesis gas generation. Ni-8YSZ and the new alternative Ni-GDC, however, have shown microstructural changes at the fuel electrode during long-term operation in humidified gas composition, with adverse effects on the overall cell stability and performance.[12–23] In SOEC operation, Ni particle agglomeration and Ni particle migration from the active electrode layer to the electrode supporting layer as well as subsequent performance loss have been observed. This migration of Ni from the electrochemically active electrode/electrolyte interface has been linked to the employed operating temperature, gas stream humidity, overpotential, and current density.

Ni-free perovskite fuel electrodes with mixed ionic and electronic conductive properties are considered as an alternative to Ni-ceramic-metal (cermet) fuel electrodes to mitigate the Ni degradation phenomena. Prerequisites for the long-term use of Ni-free ceramic materials are high stability under the applied operating conditions *e.g.* steam contents, polarization, and temperature as well as high electrocatalytic performance and sufficient electrical and/or ionic conductivities.[1] The considered fuel electrode materials include mixed ionic-electronic conducting (MIEC) perovskites such as $La_{0.75}Sr_{0.25}Cr_{0.5}Mn_{0.5}O_{3-\delta}$ (LSCM),[24] $Sr_2FeNbO_{6-\delta}$ (SFN),[25] $La_{0.4}Sr_{0.4}TiO_{3-\delta}$ (LST),[26] $(PrBa)_{0.95}(Fe_{0.9}Mo_{0.1})_2O_{5+\delta}$ (PBFM),[27] and $Sr_2Fe_{2-x}Mo_xO_{6-\delta}$ (SFMx).[28–30] Some of these alternative electrode materials still exhibit reduced ionic and/or electronic conductivity, catalytic activity, or long-term stability under operating conditions. Therefore, they cannot yet be used on an industrial scale, and further studies are needed to improve the properties, investigate, and demonstrate the material stability. SFM-based perovskites are predominantly considered due to their excellent redox stability, good catalytic performance, and reported long-term stability in fuel cell mode for symmetrical cell tests.[29,31–33] However, the long-term stability of SFM as a fuel electrode material has not been investigated beyond 100 h in humidified electrolysis for H_2 and synthesis gas production. Therefore, in this work, SFM-based fuel electrode materials and the composite ceramic–ceramic (cercer) SFM-GDC were investigated in steam- and co-electrolysis conditions for the first time

regarding performance and long-term stability of up to 500 h in 50% steam. This article is based on the work published in.[34]

2. Experimental

2.1. Powder preparation

SFM powder was prepared using a solid-state synthesis route. The corresponding precursors were $SrCO_3$ (Aldrich chem, 99%), MoO_3 (Alfa Aesar, 99%), and Fe_2O_3 (Alfa Aesar, 99%). The precursors were weighed according to the desired composition and then ball milled for 4 h at 250 rpm using zirconia balls and isopropanol (VWR, 99.8%). After drying overnight at room temperature, they were annealed at 1100 °C for 8 h in air, leading to well-crystallized phases. The obtained powders were crushed and milled again with zirconia balls and isopropanol for 8 h to obtain a mean particle size of about 1 μm (as checked using SEM). For the SFM-$Ce_{0.8}Gd_{0.2}O_{1.9}$ (GDC) composite electrode, commercial GDC powder (SOFCMAN, 99.5%) was used and weighed in a 70 : 30 ratio (SFM : GDC), then ground in acetone, and dried overnight. The powder mixture was ball-milled at 1200 rpm for 10 min. The $La_{0.58}Sr_{0.4}Co_{0.2}Fe_{0.8}O_{3-\delta}$ (LSCF) oxygen electrode powder was prepared with a modified Pechini method using previously dried La_2O_3 (Aldrich, 99%).[35]

2.2. X-ray diffraction analysis (XRD)

The powders were investigated by X-ray diffraction (XRD) with an EMPYREAN (Malvern Panalytical, Almelo, The Netherlands) with a PIXcel3D detector and Cu-Kα incident radiation. The data were recorded at room temperature before and after heating to 900 °C for 7 h in Ar-4% H_2. The data were analysed using the Rietveld refinement method with TOPAS Academic v.6 software.[36,37]

2.3. Dilatometry measurements

Measurements of the relative expansion of dense pellets (dL L^{-1}) with varied temperatures between 25–1000 °C were carried out under air using a differential dilatometer (Netzsch® 402C), to determine the Thermal Expansion Coefficient (TEC) of the materials to determine the Thermal Expansion Coefficient (TEC) of the materials between 30–800 °C.

2.4. X-ray photoelectron spectroscopy (XPS)

The samples were heated up to 900 °C with 1 °C min^{-1} in N_2 and then reduced in 100% H_2 for 72 h. Using a Phi5000 VersaProbeII (ULVAC-Phi Inc., USA) instrument, XPS analyses were carried out with an X-ray beam size of 200 μm at 15 keV and a monochromatic Al Kα irradiation at 50 W. Survey scans were recorded with a 187.5 eV analyzer pass energy in 0.8 eV steps (100 ms per step). The high-resolution analyses (10–30 eV wide range) were carried out with an analyzer pass energy of 23.5 eV in 0.1 eV steps. Referencing was performed using the SrO signal at 132.9 eV in the Sr 3d spectrum for both samples. The core peaks were analyzed using a nonlinear Shirley-type background. For evaluation, the program CasaXPS was used.

2.5. Scanning electron microscopy (SEM)

The morphology of the as-prepared and reduced SFM powders was characterized by using a Scanning Electron Microscope (SEM), (FEI Quanta FEG 650, FEI equipped with an EDS detector, USA) at 10 kV.

2.6. Transmission electron microscopy (TEM)

High-Resolution Transmission Electron Microscope (TEM) images were captured using an aberration-corrected Thermo Fischer Titan TEM at 300 kV. Elemental distribution mapping was conducted using a Hitachi HF5000, provided by Hitachi High-Technologies, Japan, and equipped with Energy Dispersive Spectroscopy (EDS) from Oxford Instruments.

2.7. *In situ* Transmission Electron Microscopy (*in situ* TEM)

The *in situ* Transmission Electron Microscopy (*in situ* TEM) sample was prepared by depositing a suspension of as-prepared SFM particles in ethanol onto MEMS-based heating chips named "Climate" from DENS solutions *via* drop-casting. The chip assembly was integrated into the DENS solutions *in situ* gas-flow and heating holder, and subsequently, the holder underwent plasma treatment. Following a successful leak test, the prepared holder was introduced into the TEM chamber. The Gas Supply System (GSS) from DENS solutions was utilized to facilitate the flow of gases through the nano-reactor cell of the *in situ* holder. *In situ* hydrogen reduction of as prepared SFM was conducted in a Thermo Fischer Titan transmission electron microscope with aberration correction at 300 kV. To eliminate any carbon impurities, the sample underwent decontamination within the nano-reactor for approximately 30 min, achieved by introducing Ar gas at a pressure of 0.95 bar (approximately 1 bar) and at 300 °C. After the decontamination process, a gas mixture consisting of Ar-3% H_2 was circulated through the nano-reactor cell of the MEMS chip at a pressure of 0.95 bar (approximately 1 bar) at a temperature of 800 °C and with a flow rate maintained at 1 ml min^{-1}. The *in situ* movies were captured using the Gatan OneView Camera at a recording rate of 3–4 frames per second, with a resolution of 2k × 2k pixels.

2.8. Conductivity measurements

The electrical conductivity of the materials was determined in the temperature range from 500 °C to 900 °C under air and hydrogen. The bar samples were sintered at 1350 °C for 6 h to prepare dense pellets. To measure the conductivity, the samples were installed in a ProboStat™ (NORECS AS, Oslo, Norway), and four-probe Direct Current (DC) measurements were conducted with an Iviumstat™ (Ivium Technologies B.V., Eindhoven, Netherlands) from 900 °C to 500 °C in steps of 50 °C with the heating and cooling rate of 1 °C min^{-1}. After the measurements in air, the gas atmosphere was changed to 100% H_2. To characterize the conductivity in 100% H_2, the same measurement settings were employed between 900 °C to 650 °C in steps of 50 °C. The temperature limit of 650 °C was set due to safety reasons.

2.9. Cell preparation

Single cells SFM/GDC/8YSZ/GDC/LSCF and SFM-GDC/GDC/8YSZ/GDC/LSCF were prepared for electrochemical characterization. The slurries were prepared by mixing the SFM powder, the gadolinium doped ceria *i.e.*, GDC powder, and the mixed powders of SFM and GDC each with a binder solution comprised of 3 wt% ethyl cellulose (binder) dissolved in α-terpineol (dispersant). Afterward, the slurries were mixed in a planetary vacuum mixer (THINKY Mixer ARV-310, C3 Prozess-und Analysentechnik GmbH, Germany) and further homogenized by roll milling. To prepare the cells, the layers were screen printed (EKRA screen printing Technologies), dried, and then sintered. First, GDC layers (thickness ~3–5 μm, ∅ ~18 mm) were screen printed symmetrically on both sides of the dense ~250 μm thick 8 mol% yttria-stabilized zirconia (8YSZ) supports with a diameter of ~20 mm (Kerafol®, Germany). The GDC layer was sintered at 1375 °C for 1 h in air. This GDC buffer layer was deposited to prevent the formation of insulating secondary phases resulting from the reactivity between the electrodes and 8YSZ. The SFM layer (thickness ~15–20 μm, ∅ ~12 mm) was deposited subsequently using the same method and sintered at 1150 °C for 2 h under air. The optimized sintering temperature (1150 °C) showed a homogenous porous electrode microstructure. The same sintering conditions were used to prepare the SFM-GDC composite electrode. The LSCF oxygen electrode (thickness ~30 μm, ∅ ~12 mm) was screen-printed and sintered at 1080 °C for 3 h.[38] In the last step, an Au contact layer (thickness ~4–5 μm, ∅ ~ 12 mm) was deposited on the fuel electrode and sintered at 900 °C for 1 h in air.

2.10. Electrochemical characterization

The single-cell measurements were performed using 8YSZ-supported single cells with the compositions SFM/GDC/8YSZ/GDC/LSCF and SFM-GDC/GDC/8YSZ/GDC/LSCF. The cells were measured in a two-electrode, four-probe ProboStat™-setup (Norwegian Electro Ceramics® NORECS, Oslo, Norway) placed in an automated test rig (EBZ GmbH, Dresden, Germany). The intermixing of gas streams was prevented with an Au gasket inserted between the cell's oxygen side and the inner ceramic gas tube. Gases were set with Mass Flow Controllers (MFCs, Bronkhorst Nord®, Kamen, Germany) and the fuel gas was led through a temperature-regulated water gas bubbler for humidification.[39,40] The current collectors were made of Pt mesh for the oxygen and Au mesh for the fuel side. Before the experiments, the fuel electrode was reduced step-wise in H_2 as described previously.[39] Electrochemical impedance spectra and current–voltage characteristics were recorded with a Vertex.5A Potentiostat/Galvanostat system (Ivium Technologies®, Eindhoven, Netherlands) in the temperature range from 750 °C to 900 °C. The current–voltage characteristics were recorded potentiostatically at a scan rate of 10 mV·s^{-1} from 0.6 V (fuel cell mode) to 1.5 V (electrolysis mode). Impedance spectra were recorded with an AC amplitude of 50 mA in the frequency range from 110 kHz down to 0.11 Hz at Open Circuit Voltage (OCV) and from 0.7 V to 1.4 V. The long-term stability tests were carried out at an applied current density of −0.3 A cm^{-2} at

a temperature of 900 °C under the steam electrolysis conditions, *i.e.*, 50% H_2O + 50% H_2 gas flow at the fuel electrode, and airflow at the oxygen electrode with a total flow rate of 9 l h^{-1}. After the electrochemical characterization, the microstructural changes were analyzed.

3. Results and discussion

3.1. Material characterization

The as-prepared powder was characterized in an XRD study in air and after reduction in Ar-4% H_2 for 7 h at 900 °C (Fig. 1a, b and Tables S1 and S2). The XRD of the as-prepared SFM powder shows distinct secondary phase formation of 37 wt% $SrMoO_4$ (space group: $I4_1/a$, ICSD-99089) in addition to two phases of $Sr(Fe_{0.8}Mo_{0.2})O_3$ (space group: $Pm\bar{3}m$, ICSD 191551) with 42 wt% (α = 3.929 Å) and 21 wt% (α = 3.910 Å). This result is consistent with previous observations on the phase stability of $Sr_2FeMoO_{6-\delta}$.[41–43] Phase diagram studies on the composition

$Sr_2FeMoO_{6-\delta}$ showed that the solid solubility of Mo in air is limited to 17 at% Mo, wherefore the $Sr_2FeMoO_{6-\delta}$ composition is not obtained in air and the secondary phase $SrMoO_4$ is observed.[43] After annealing the oxidized sample under reducing conditions at 900 °C for 7 h, the room temperature X-ray diffraction (XRD) data showed that the perovskite phases were converted into several mixed phases. The reduced sample was composed of 27 wt% Ruddlesden–Popper phase Sr_3FeMoO_7 (space group: $I4/mmm$, ICSD-156787), 36 wt% simple cubic perovskite $Sr(Fe_{0.8}Mo_{0.2})O_3$ (space group: $Pm\bar{3}m$, ICSD-191551), 33 wt% double perovskite $Sr_2(Fe_{1.33}Mo_{0.66})O_{5.88}$ (space group: $Fm\bar{3}m$, ICSD-168704) with superstructure reflexed at 19° and 37.9°, as well as around 4 wt% exsolved iron (Fe^0). The perovskite phase $SrFe_{1-x}Mo_xO_{3-\delta}$ (x = 0.3) has been reported to exhibit mixed oxygen ionic and electronic conducting properties.[41,44–46] The semiconducting and oxygen-deficient Ruddlesden–Popper phase $Sr_3FeMoO_{7-\delta}$ exhibited mixed valence states for Fe and Mo ions in X-ray Absorption Near Edge
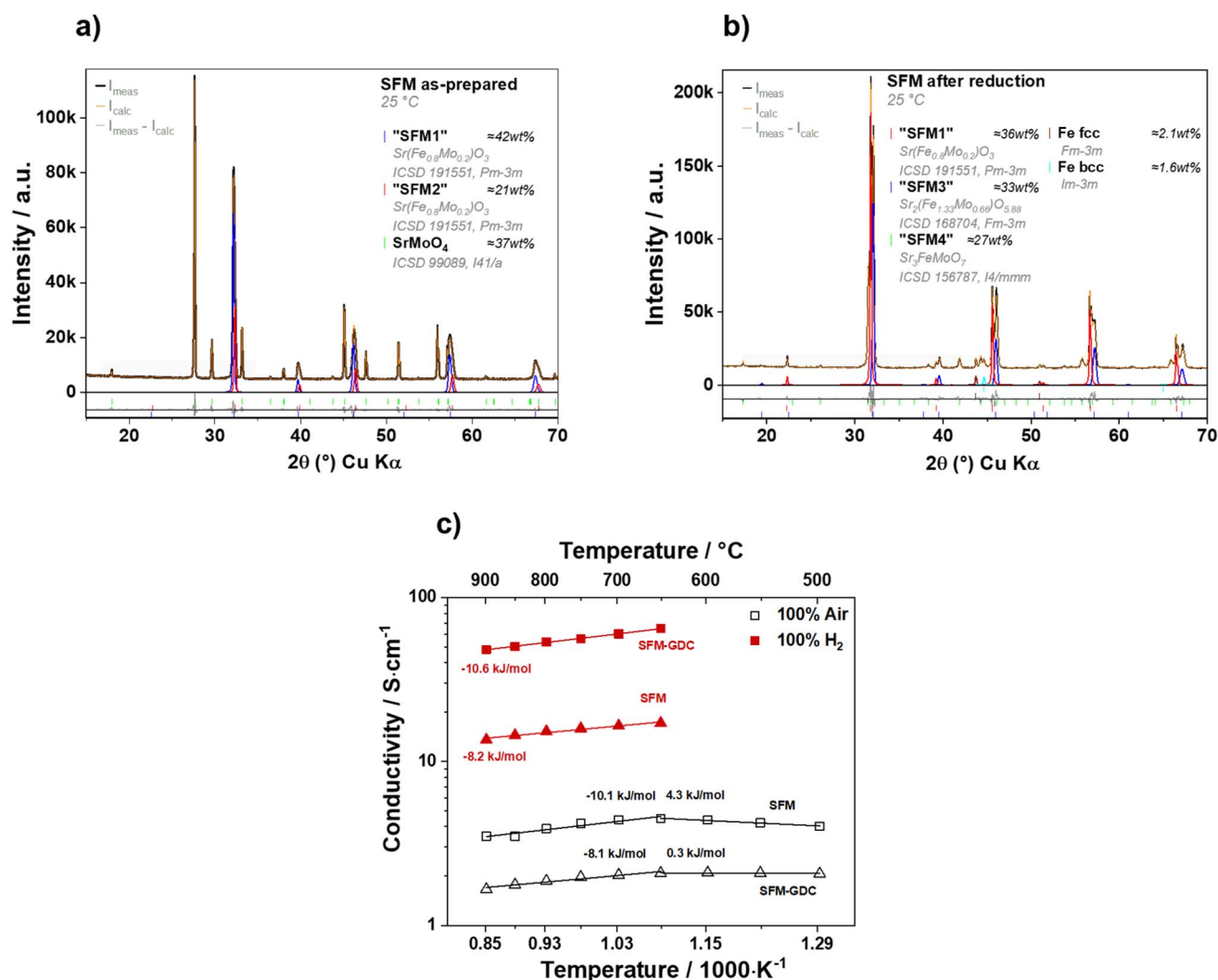

Fig. 1 Room-temperature powder XRD pattern with Rietveld refinement analysis of the as-prepared SFM in (a) air and (b) after reduction in 100% H_2 for 7 h at 900 °C (Rietveld data can be found in Table S1). (c) Conductivity measurements in the temperature range of 500–900 °C in air and hydrogen for SFM and the composite sample SFM-GDC. The measurements in hydrogen were conducted down to 650 °C for safety reasons.[1]

Structure (XANES), neutron diffraction, and Mössbauer data, which hints at sufficient electronic conductivity.[47,48]

The total conductivity was measured with four probe Direct Current (DC) measurements in air and hydrogen atmospheres at operating temperatures between 500 °C and 900 °C and is displayed as total electrical conductivity σ vs. $1000/T$ in Fig. 1c. SFM and SFM-GDC exhibit semiconducting behavior in air up to the maximum conductivity at 650 °C with 4.5 S cm^{-1} and 2.1 S cm^{-1}, respectively. At higher temperatures, the conductivity behavior is pseudo-metallic and decreases up to 3.5 S cm^{-1} for SFM and 1.7 S cm^{-1} for SFM-GDC at 900 °C. The electrical conductivity in air is lower than for SFM due to SrMoO$_4$, which exhibits conductivities several magnitudes smaller than SFM.[49] After 24 h in H$_2$, a conductivity of 13.5 S cm^{-1} was achieved for SFM at 900 °C, while the composite material SFM-GDC showed pseudo-metallic behavior as well as with a higher conductivity of 48.1 S cm^{-1} at 900°. The observed mixed perovskite phases of SFM in H$_2$ atmosphere are highly mixed ionic-electronic conducting, while the pseudo-metallic behavior of SFM has been previously observed for SrFeO$_{3-\delta}$-based perovskite materials and was related to the loss of oxygen during the heating procedure and the partial delocalization of mobile electronic charge carriers.[43] At high oxygen partial pressures (pO$_2$), the electronic holes are the dominant charge carriers, however, in reducing atmosphere the ferromagnetic double perovskite SFM exhibits electrical conductivity and oxide-ion conductivity. Although the oxygen vacancy diffusion rate increases with temperature, the electrical conductivity mechanism is related to the hopping of small polarons associated with the mixed-valent redox relation shown in eqn (5).[50] Despite an increased ionic conductivity of ferrite-molybdates in reducing atmosphere, it remains negligible compared to the predominant electrical conductivity.[50]

$$Fe^{3+} + Mo^{5+} \rightleftarrows Fe^{2+} + Mo^{6+} \tag{5}$$
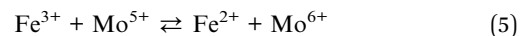
Gadolinium doped ceria (GDC) exhibits good ionic conductivity ($\sim$0.1 S cm^{-1} at 800 °C) in air and develops mixed ionic and electronic conductivity due to the reduction of Ce^{4+} to Ce^{3+} in reducing conditions.[51–54] This mechanism additionally increases the total conductivity of SFM-GDC under reducing conditions.

SFM as well as SFM-GDC exhibit higher conductivities in reducing atmosphere ($\sigma_{\text{SFM}} = 13.5$ S cm^{-1} at 900 °C, $\sigma_{\text{SFM}} = 15.3$ S cm^{-1} at 800 °C; $\sigma_{\text{SFM–GDC}} = 48.1$ S cm^{-1} at 900 °C, $\sigma_{\text{SFM–GDC}} = 53.3$ S cm^{-1} at 800 °C) than other perovskite materials such as La$_{0.75}$Sr$_{0.25}$Cr$_{0.5}$Mn$_{0.5}$O$_3$ (1.5 S cm^{-1} at 900 °C in 5% H$_2$–Ar)[55] and Sr$_2$MgMoO$_{6-\delta}$ (4 S cm^{-1} in 5% H$_2$–Ar, 9.3 S cm^{-1} at 800 °C in H$_2$),[56] which have also been considered promising alternative fuel electrode materials. In comparison to SFM, conductivities for the double perovskite Sr$_2$FeNbO$_{6-\delta}$ were also observed to be lower at 850 °C with 0.05 S cm^{-1} in air and 2.215 S cm^{-1} in reducing conditions of 5% H$_2$ + 95% Ar.[57]
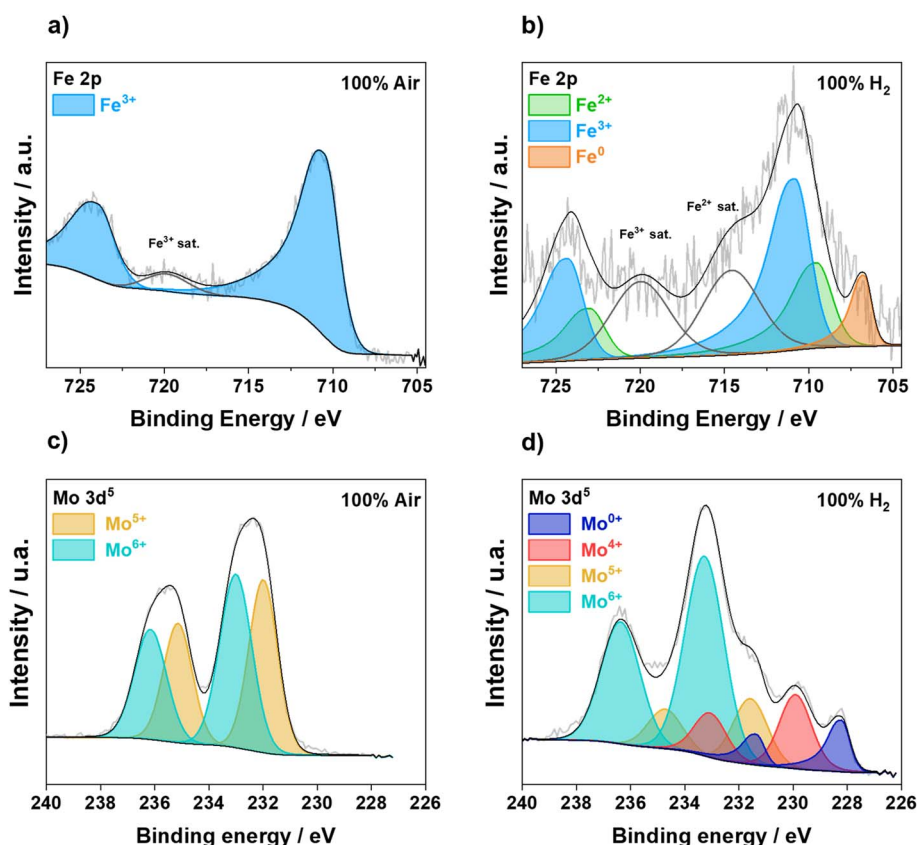

Fig. 2 Selected XPS scans of SFM samples sintered in air and after reduction in 100% H$_2$. Fe spectrum (a) before and (b) after reduction. Mo spectrum (c) before and (d) after reduction.

XPS measurements were carried out on the surface of bar samples to study the oxidation states of iron and molybdenum in SFM at room temperature for oxidized (Fig. 2a and c) and reduced samples (Fig. 2b and d). The complete XPS analysis results are listed in Tables S3 and S4. The analysis of Fe 2p confirms that the majority of the iron in SFM exists as Fe^{3+} (binding energy = 710.4 eV, 723.9 eV) in the as-prepared sample. The reported mixed valence state of $Fe^{3+} \leftrightarrow Fe^{2+}$ (709.8 eV) could not be confirmed due to low measurement intensities. In comparison, the XPS scan of iron for the reduced sample shows the distinct mixed oxidation states of Fe^{2+} (709.5 eV, 723.0 eV), Fe^{3+} (~710.8 eV, 724.3 eV), as well as metallic iron Fe^0 (706.7 eV). These results are consistent with previous studies of other SFM-based perovskite materials and highlight the formation of metallic iron in the sample surface (Fe particle exsolution).[58–60] The Mo 3d XPS spectra show two broad peaks for the oxidized sample, which could be fitted with two valence states of Mo^{6+} (231.9 eV and 235.0 eV) and Mo^{5+} (232.9 eV and 236.0 eV). As anticipated from eqn (5), the Mo^{5+} valence is coupled with Fe^{3+} and is slightly predominant compared to Mo^{6+} in the oxidized sample. After the reduction of the SFM sample, the Mo^{6+} (231.6 eV and 234.7 eV) and Mo^{5+} (233.3 eV and 236.4 eV) are still present in the sample. However, caused by the reduction with H_2, two additional species can be observed in the Mo 3d of the reduced sample, which correspond to Mo^{4+} (229.9 eV and 233.1 eV) and Mo^0 (228.2 eV and 231.7 eV).[61]

Iron-based double perovskite structures have been observed to exsolved highly catalytic active and conductive iron nanoparticles at the material surface when exposed to strongly reducing conditions.[62] During the formation of these additional catalytic sites, the perovskite structure that tightly anchors these particles transforms into so-called Ruddlesden–Popper phases (RP).[30,59,63] The metallic iron in the reduced XPS measurements hinted that Fe nanoparticles are exsolved during the reduction of SFM.

To support the obtained data, high-resolution Scanning Electron Microscopy (SEM) and Transmission Electron Microscopy (TEM) images were obtained (Fig. 3 and 4). Fig. 3a and b illustrate the secondary electron SEM images of the SFM samples before and after reduction, respectively. The as-prepared SFM powder particles show a smooth and homogenous surface. In contrast, the featured surface of the reduced sample is rough and uneven likely attributed to the sub-micron nanoparticle surface. To elucidate the nature and composition of the growth on the reduced sample surface, EDS mapping was conducted. Fig. 3c depicts a typical High-Angle Annular Dark-Field (HAADF)-STEM image of the reduced SFM, accompanied by its corresponding elemental mapping in Fig. 3d–g. The Z-contrast difference highlighted by green dotted boxes in Fig. 3c, is attributed to thickness effects, possibly indicating the presence of internal nanopores within the particles.[64,65] Fig. 3e shows the presence of Fe-rich exsolution measuring 10–70 nm.
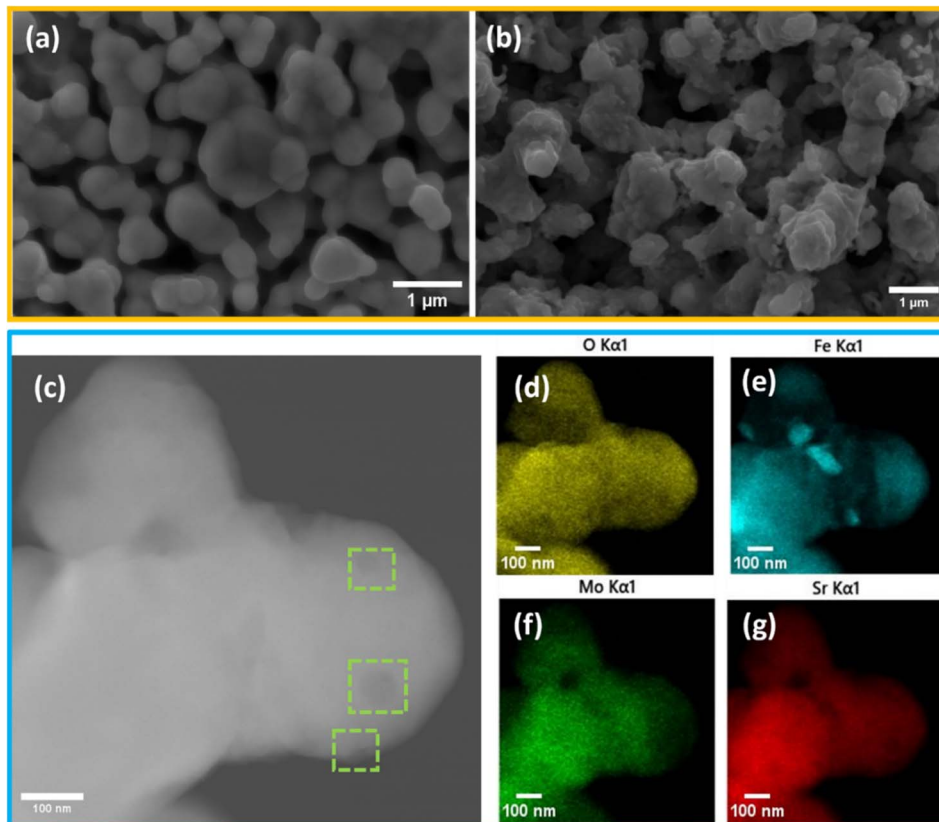

Fig. 3 SEM image of (a) as-prepared and, (b) reduced SFM powders. (c) High magnification HAADF-STEM image of the reduced SFM particle illustrating the contrast features in green boxes and (d–g) elemental mapping of the corresponding particle.
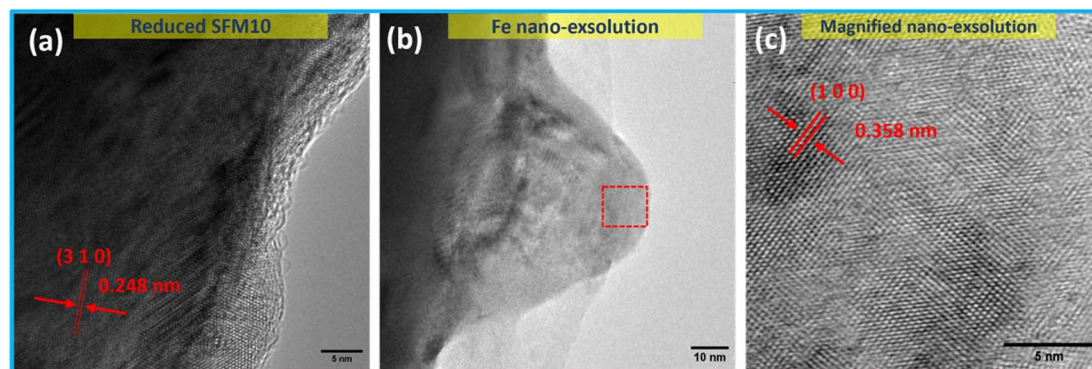
Fig. 4 (a) HRTEM image of reduced SFM, TEM image of (b) reduced SFM with exsolution illustrating the anchoring effect of the Fe nano-exsolution with the SFM matrix, (c) HRTEM image of Fe nano-exsolution of the inset marked with red box depicted in (b).

The elemental distribution of all other elements is relatively even throughout the particle.

The TEM image in Fig. 4b serves to affirm the presence of Fe-rich nano-exsolutions on the SFM particle surface post-reduction. The HRTEM image additionally reveals the strong anchoring effect between the exsolved Fe nanoparticle and the perovskite substrate. This anchoring effect contributes significantly to the surface stability of the electrode material during operation as they effectively prevent the sintering and agglomeration of metal nanoparticles at higher temperatures. Furthermore, this anchoring enhances the catalytic activity of the nanoparticles and imparts resistance to hydrocarbon coking, augmenting the overall performance of the system.[66–68] The lattice spacing information was evaluated from the HRTEM images. The TEM image in Fig. 4a illustrates the lattice spacing of the reduced SFM matrix having a 0.248 nm lattice gap, corresponding to the plane (3 1 0) of $Sr_2 (Fe_{1.33} Mo_{0.66})O_{5.88}$ (space group: $Fm\bar{3}m$, ICSD-168704). In Fig. 4c, the 0.358 nm lattice spacing of Fe nanoparticle exsolution matches the (1 0 0) plane of FCC-gamma-Fe (space group: $Fm\bar{3}m$, ICSD-43096). The substrate has a lattice spacing of 0.276 nm, which corresponds to the (1 1 0) plane of $Sr(Fe_{0.8}Mo_{0.2})O_3$ (space group: $Pm\bar{3}m$, ICSD-191551). Further information on the lattice parameters of the as-prepared sample, the reduced sample and the Fe-rich exsolution has been provided in supplementary Fig. S5 and S6. The lattice spacing from the HRTEM images provides information regarding the phases present in the as-prepared and reduced states of the SFM particles, respectively. Fig. S4a illustrates the HRTEM image of as-prepared SFM particles and exhibits lattice spacings of 0.276 nm, which corresponds to the (1 1 0) plane of $Sr(Fe_{0.8}Mo_{0.2})O_3$ (space group: $Pm\bar{3}m$, ICSD-191551). In Fig. S4b, the lattice spacings of reduced SFM particles exhibit a lattice spacing of 0.321 nm, corresponding to the planes (1 0 3) of Sr_3FeMoO_7 (space group: $I4/mmm$, ICSD-156787).

The results obtained from the TEM lattice parameter calculations support the data obtained from the XRD characterization of both as-prepared and reduced SFM particles. In the supplementary Fig. S7a–i, snapshots of different time stamps taken from the *in situ* reduction videos are provided and discussed in detail in the SI (Video S1). These figures depicting the Fe nano-exsolution growth offer insights into the underlying mechanism of their growth. Further, experiments have documented the initiation of nano-exsolution growth at multiple surface regions (Videos S2 and S3).

The compatibility of the cells' Thermal Expansion Coefficients (TECs) is a prerequisite for further use of SOC materials. The TECs were calculated from the slope of dilatometry measurements in air for SFM and SFM-GDC and are 13.8×10^{-6} °C^{-1} and 12.9×10^{-6} °C^{-1} respectively. These values are in the range of other state-of-the-art SOC materials like 8YSZ and GDC, which indicates their good thermo-mechanical compatibility.[69–72]

3.2. Electrochemical performance

The fuel electrode materials SFM and SFM-GDC were characterized in steam electrolysis and co-electrolysis conditions between 750 °C and 900 °C. The experimental Open Circuit Voltage (OCV) was compared for all operating conditions to the theoretical values derived by the Nernst equation to rule out gas leaks. The experimental deviation from the theoretical potential in steam electrolysis conditions at 900 °C amounted to 1.8 mV, which is a deviation of less than 1%. Fig. 5a and b display the respective current–voltage characteristics recorded at 800 °C and 900 °C as well as the impedance measurements at OCV and 900 °C. The performance of SFM at 1.5 V as observed in the current–voltage characteristics is only slightly higher compared to SFM-GDC. The single cell with the SFM fuel electrode achieved -1.26 A cm^{-2} and -1.27 A cm^{-2} for steam and co-electrolysis conditions, respectively. The SFM-GDC fuel electrode achieved slightly lower current densities in steam and co-electrolysis with -1.24 A cm^{-2} and -1.27 A cm^{-2}, respectively (Table 1 and Fig. 5a and b). With decreasing temperature, the performance difference between SFM and SFM–GDC increases, and at 750 °C, -0.48 A cm^{-2} with SFM and -0.37 A cm^{-2} with SFM-GDC were achieved in steam electrolysis. The state-of-the-art Ni-8YSZ fuel electrode measured in the same conditions exhibited lower performance for H$_2$O, and co-electrolysis in comparison to the SFM and SFM–GDC fuel electrodes at 900 °C (-0.91 A cm^{-2},[73] and -1.06 A cm^{-2} (ref. 73)). However,
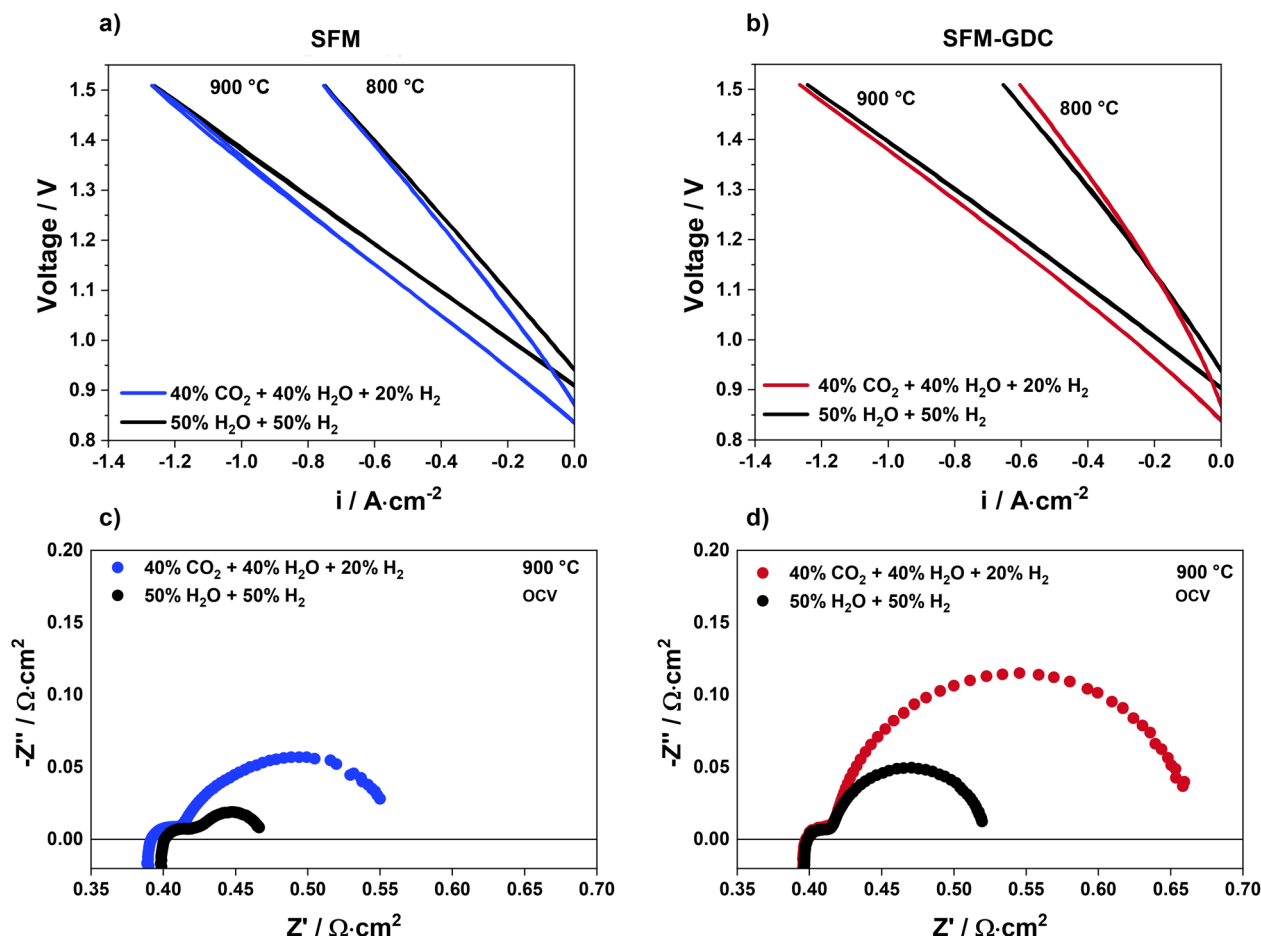
Fig. 5 *I–V* curves at 800 °C and 900 °C for SFM in (a) steam electrolysis and co-electrolysis compared to (b) the composite SFM-GDC in steam electrolysis and co-electrolysis conditions. The corresponding impedance spectra at 900 °C recorded in steam electrolysis and co-electrolysis are given for (c) SFM and (d) the SFM-GDC composite.

Table 1 Comparison of electrochemical performance for SFM-based fuel electrodes compared to state-of-the-art solid oxide cell materials[a]

Fuel electrode	Test conditions @ 900 °C	R_P @ OCV/Ω cm^2	i @1.5 V/A cm^{-2}	Ref.
Ni-8YSZ	50% H_2O + 50% H_2	0.17	−0.91	73
	40% H_2O + 40% CO_2 + 20% H_2	0.20	−1.06	73
Ni-GDC	50% H_2O + 50% H_2	0.06	−1.31	73
	40% H_2O + 40% CO_2 + 20% H_2	0.09	−1.37	73
SFM	50% H_2O + 50% H_2	0.07	−1.26	This work
	40% H_2O + 40% CO_2 + 20% H_2	0.17	−1.27	This work
SFM-GDC	50% H_2O + 50% H_2	0.13	−1.24	This work
	40% H_2O + 40% CO_2 + 20% H_2	0.27	−1.27	This work

[a] All cells were prepared in the configuration FE/GDC/8YSZ/GDC/LSCF with the same precursor materials, pastes and supported on a 250 μm thick 8YSZ electrolyte. GDC: $Ce_{0.8}Gd_{0.2}O_{1.9}$, 8YSZ: 8 mol% YSZ, LSCF: $La_{0.58}Sr_{0.4}Co_{0.2}Fe_{0.8}O_{3-\delta}$.

electrolyte-supported Ni-GDC fuel-electrode containing single cells exhibit higher current densities at 900 °C and 1.5 V with −1.31 A cm^{-2}, and −1.37 A cm^{-2} in steam, and co-electrolysis conditions.[74] The results obtained in this work for SFM (−0.67 A cm^{-2}) and SFM-GDC (−0.62 A cm^{-2}) at 850 °C and 1.3 V are in the range of values previously obtained for the single cell with SFM-SDC electrode (SFM-SDC (−$Sm_{0.2}Ce_{0.8}O_{1.9}$)/LCO/LSGM/ SDC-LSCF). The data showed a current density of −0.64 A

cm^{-2} at 850 °C and 1.3 V with 42% H_2O + 58% H_2 fuel gas mixture.[30]

In Fig. 5c and d, the impedance spectra measured in steam and co-electrolysis at 900 °C are shown. Under OCV conditions, both SFM and SFM–GDC cells exhibit higher polarization resistance in co-electrolysis mode compared to steam electrolysis mode. In addition, the Area-Specific Resistance (ASR) of the SFM-GDC composite electrode increases by 1423 mΩ cm^2 for

steam- and 3164 mΩ cm^2 in co-electrolysis atmosphere when decreasing the temperature from 900 °C to 750 °C. The SFM electrode shows a smaller increase in ASR with 744 mΩ cm^2 and 1352 mΩ cm^2 for steam and co-electrolysis, respectively. The ASR is composed of the ohmic R_Ω and polarization resistance R_P. The ohmic resistance R_Ω is obtained by the interception of the Nyquist plot with the real impedance axis (abscissa) at higher frequencies. The activation energy for R_Ω is determined based on the slope of the Arrhenius equation and ranges between 50–56 ± 5 kJ mol^{-1}. This closely concurs with values reported in the literature for the ionic conductivity in YSZ electrolyte films and suggests that the primary contribution to R_Ω is the 250 μm thick 8YSZ electrolyte.[74–76]

3.2.1. Electrochemical impedance characterization

3.2.1.1 Equivalent circuit model evaluation. The Nyquist plots for the single button cells with SFM and SFM-GDC composite fuel electrodes broadly show two contributions *i.e.* low-frequency and high-frequency contributions (Fig. 6a–d). To deconvolute the underlying frequency-dependent physical processes at the electrodes, impedance spectra were taken with varied temperature, fuel composition and oxygen partial pressure and subsequently evaluated by Distribution of Relaxation Times (DRT) analysis (Fig. 6e–h). The number of time constants observed in the DRT spectra were used to establish an Equivalent Circuit Model (ECM) with an appropriate number of passive elements to fit the impedance spectra.

The exemplary DRT spectra show that four underlying time constants P1, P2, P3, and P4 in the analyzed frequency range make up the total cell impedance given in the experimental Nyquist plots. Therefore, the final ECM consists of four R//Q elements connected in series including an inductor (I) and a serial resistor (R_Ω). The inductance I and series resistance (R_Ω) account for the wires' inductivity and the ohmic losses contributed by the electrolyte and electrodes (Fig. 7a). The quality analysis of the Complex Non-Linear-Least-Square (CNLS) fit with this ECM is given in the Fig. 7b–d by comparing the DRT and Nyquist plots of experimental and fitted data and shows qualitatively good agreement. Furthermore, the relative residuals as well as the low (chi-square) error of 10^{-8} between the fitted and experimental data indicate an acceptable ECM.

3.2.1.2 Temperature variation. The performance of single cells with SFM/GDC/8YSZ/GDC/LSCF and SFM-GDC/8YSZ/GDC/ LSCF was evaluated in steam electrolysis (50% H_2O + 50% H_2) and co-electrolysis (40% H_2O + 40% CO_2 + 20% H_2) atmosphere between 750 °C and 900 °C in steps of 25 °C to characterize the thermally activated processes. The polarization resistances are given in Table S8. The corresponding Nyquist plots in Fig. 6a–d show an increase in the low- and high-frequency impedance contributions with decreasing temperature, indicating thermally activated processes. All these impedance diagrams were fitted by four R//Q elements including I and R_Ω. The resistances obtained for the four different processes are shown in Fig. 7 and corroborated by DRT spectra as a function of temperature for SFM and SFM-GDC under steam- and co-electrolysis conditions (Fig. 6).

As can be seen from the DRT spectra and the resistance analysis, the predominant physical process, which corresponds to the rate-limiting step is P4 (R_{RQ4}, 2–0.1 Hz) for both steam- and co-electrolysis conditions (Fig. 7). The activation energy of this low-frequency process is between 118 ± 12 kJ mol^{-1} to 131 ± 16 kJ mol^{-1} for cells with the SFM fuel electrode in steam and co-electrolysis. The cells with an SFM-GDC fuel electrode exhibited activation energies from 134 ± 2 kJ mol^{-1} to 149 ± 5 kJ mol^{-1}. Physical processes suggested in this frequency range include gas conversion as well as diffusion processes at the fuel electrode side. These processes, however, exhibit very low thermal activation and therefore cannot be attributed to P4.[40,77,78] Very few studies based on perovskite fuel electrodes show individual process analysis including activation energies, suggest adsorption and/or dissociation processes at the SFM-based fuel electrode in this frequency range.[58,66,79–82] As shown by Fig. S9, the process that is mainly influenced by polarization is also P4.[83] This is an indication of a charge transfer process that has been observed for MIEC electrodes around 1–2 Hz[84] with an activation energy of around 107–126 kJ mol^{-1}.[75] However, the investigated data of P4 showed no clear Butler–Volmer behavior, which suggests that another process might overlap in this frequency range. The other processes P1 (2000–1000 Hz), P2 (500–100 Hz), and P3 (100–10 Hz) also exhibit a temperature dependency and a frequency shift with increasing operation temperature.

The observed high-frequency contribution P1 is modelled by R_{RQ1} and shows similar activation energies of 153 kJ mol^{-1} in steam and co-electrolysis for SFM and SFM-GDC fuel electrodes. The described frequency range (Table 2) and the high activation energy have been previously attributed to an electrode charge-transfer process at the LSCF oxygen electrode.[75,85–87] The middle to high-frequency process modelled by R_{RQ2} (500–100 Hz) shows activation energies between 120 – 130 kJ mol^{-1} for steam and co-electrolysis. The thermally influenced process in this frequency range has been attributed to the surface exchange kinetics and oxygen diffusion in the bulk and at the surface of the LSCF electrode.[85]

The mid to low-frequency process given by R_{RQ3} (P3, 100–10 Hz) shows an E_A highly influenced by the choice of fuel electrode material. For single cells with an SFM-GDC electrode, this process exhibits an activation energy of around 206 ± 5 kJ mol^{-1} to 222 ± 8 kJ mol^{-1}. For SFM, however, the activation energy is around (72 ± 16 kJ mol^{-1}) for steam and (96 ± 20 kJ mol^{-1}) for co-electrolysis. The significant deviation in activation energies indicates that the variation of fuel electrode material influences the process resistance R_{RQ3} in this frequency range. Previous studies suggested an overlap of fuel electrode and oxygen electrode mechanisms *e.g.*, transport processes.[85] Adsorption and diffusion processes of oxygen on the LSCF electrode surface observed in the mid-to low-frequency have shown an activation energy of 192 ± 12 kJ mol^{-1}. This is in range with the measured results for the composite SFM-GDC cell. The lower activation for cells with the SFM fuel electrode shows that another process is predominant in contrast to the SFM-GDC fuel electrode. A middle frequency process (~100 Hz) has been related previously to oxide ion transport from bulk to surface as well as across the
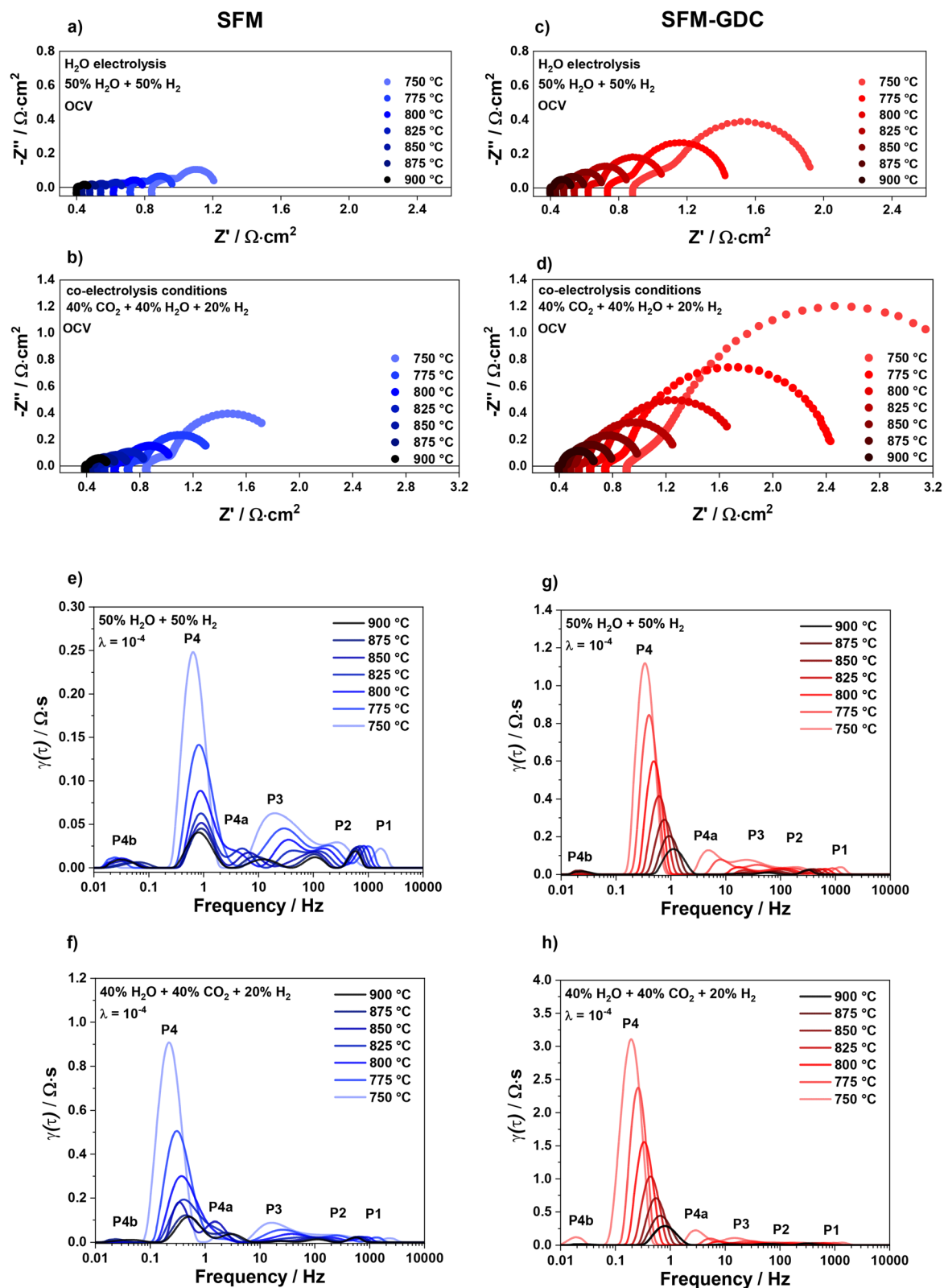
Fig. 6 Impedance spectra with a variation of temperature measured at OCV between 750 °C and 900 °C SFM in (a) steam electrolysis and (b) co-electrolysis conditions as well as SFM-GDC (c and d). In comparison, the corresponding spectra as a function of temperature for (e and f) SFM and (g and h) SFM-GDC.
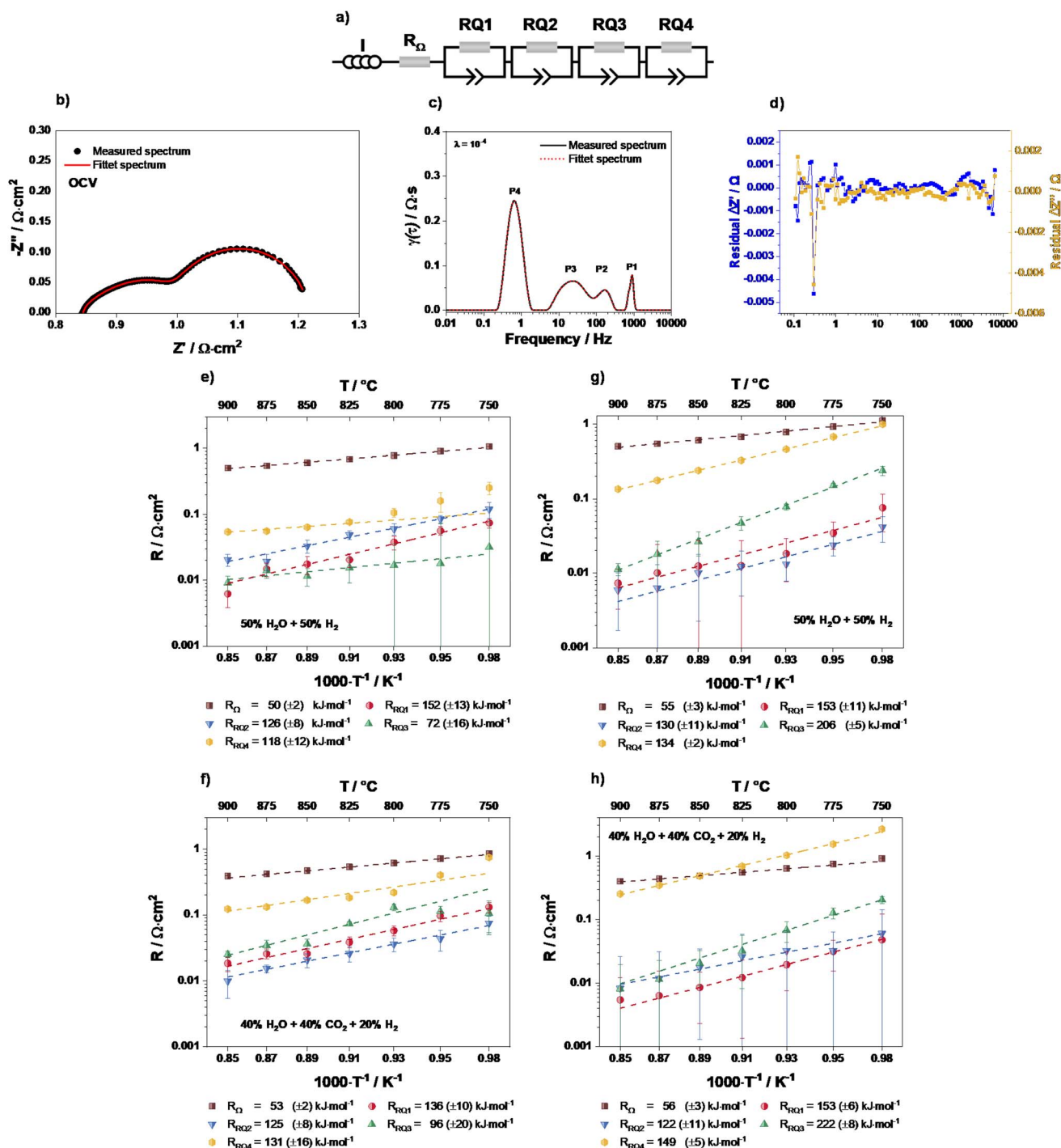
Fig. 7 (a) Equivalent circuit model (ECM) used for the complex non-linear-least-square (CNLS) fit of the experimental impedance data. (b) Distribution of relaxation times (DRT) of experimental and fitted impedance data for SFM at 750 °C in 50% H_2O + 50% H_2 recorded at OCV. (c) Nyquist plot of the experimental data and corresponding fit. (d) The corresponding residual of the fitted data to verify the quality of the CNLS fit. Temperature-dependent process resistance analysis measured at OCV from 900 °C to 750 °C in (e) steam electrolysis, and (f) co-electrolysis for SFM well as for the composite SFM-GDC in (g) steam and (h) co-electrolysis.

electrolyte/electrode interface with 100 kJ mol^{-1}.[82,84,88] A decreased activation energy for the mid-frequency process could also suggest an influence of transport processes in the fuel and oxygen electrode.[85]

3.2.1.3 Gas variation at the fuel and oxygen electrode. The in-depth process analysis was further extended by the characterization of the fuel gas influence on the impedance data. As shown in Fig. S10a and b, the concentration of steam and hydrogen in the operating atmosphere was varied, and the

Table 2 Suggested process contribution to the polarization resistance and their equivalent frequency ranges for electrolyte-supported single cells consisting of SFM(-GDC)/GDC/8YSZ/GDC/LSCF

Time constant/process	Frequency range/Hz	Dependencies	Assignment
P1 (R_{RQ1})	2000–900	Temperature	Charge transfer at LSCF oxygen electrode
P2 (R_{RQ2})	400–100	Temperature	Surface exchange kinetics and O^{2-} diffusion in the bulk and at the surface of LSCF
P3 (R_{RQ3})	100–10	Temperature, medium pH_2O (FE)	Adsorption, desorption, transport processes in the fuel and oxygen electrode
P4 (R_{RQ4})	2–0.1	Temperature, high pH_2O (FE)	Charge transfer at the SFM(-GDC) fuel electrode

impedance spectra were recorded at OCV and 900 °C. The results emphasize that an increase in H_2 has no impact on the ohmic resistance, as expected, and neither on the high-frequency arc. The main influence is observed in the mid-to-low-frequency region with a decreased polarization resistance with increasing pH_2O from 73 mΩ cm^2 at 30% H_2O + 70% H_2 to 82 mΩ cm^2 with 50% H_2O + 50% H_2. The DRT analysis of the impedance data in Fig. S10b exhibits that the main impact of the fuel gas variation is attributed to P3 and P4 in the mid-to-low-frequency regions. The peaks P1 and P2 are not dependent on a variation in fuel gas compositions.

The oxygen partial pressure on the oxygen electrode side was additionally varied at 900 °C in steam electrolysis conditions of 50% H_2O + 50% H_2 between 21% O_2 and 3% O_2 balanced with N_2. The impedance spectra measured at OCV are displayed in Fig. S10c and were further analyzed to discern the influence of the oxygen partial pressure pO_2 on the process (resistances) P1, P2, P3, and P4. The corresponding DRT spectra in Fig. S10d are plotted as a function of pO_2 and show small changes in the process peaks with varied pO_2 from 21% to 3%. P1, P2, P3, and P4 show a minimal shift to higher frequency. In addition, the shoulder peak P4a is only observable at a low pO_2 of 3%. To get further insight regarding the process of the oxygen electrode, the impedance results of single cells were compared with those of a symmetrical LSCF cell.[75] The results showed that for symmetrical LSCF/GDC/8YSZ/GDC/LSCF cells, the peaks P1, P2 and partially P3 can be assigned to processes at the oxygen electrode side. Below 21% O_2, the process P4 has shown a small contribution of the oxygen gas diffusion resistance. The influence of pO_2 on P3 and P4 is difficult to discern in single cells due to the great influence of the fuel electrode on these processes, leading to an overlap.

To conclude, the processes P1 and P2 are thermally activated processes attributed to the LSCF oxygen electrode charge transfer (P1, 2000–900 Hz) and surface exchange processes (P2, 400–100 Hz). The mid to low-frequency process P3 (100–10 Hz) exhibits the highest change in activation energy with a change in fuel electrode materials. For single cells with an SFM-GDC electrode, activation energies varied around 210 kJ mol^{-1}, while the same process showed activation energies of 72–96 kJ mol^{-1} depending on the measurement conditions. In addition, a light impact of the oxygen content below 21% was observed for this process. P3 was therefore assigned to the adsorption and diffusion processes and transport processes of the fuel and oxygen electrode overlapping in this frequency region. The

process P4 (2–0.1 Hz) has been identified as the rate-limiting step in steam- and co-electrolysis. The observed activation energies and the impact of polarization on this process led to the assignment of P4 to the fuel electrode charge transfer process.

3.3. Long-term stability tests in steam electrolysis

3.3.1. Electrochemical analysis. The Electrolyte-Supported Single Cells (ESCs) composed of SFM(-GDC)/GDC/8YSZ/GDC/LSCF were electrochemically tested under a constant load of −0.3 A cm^{-2} at 900 °C in steam electrolysis conditions for up to 500 h to investigate and quantify the degradation behavior. The resulting degradation curves are displayed in Fig. 8a. As can be seen, the cell with an SFM fuel electrode is stable for up to 50 h, after which the voltage increases strongly with a degradation rate of around 0.457 mV h^{-1} to 0.765 mV h^{-1}. In comparison, the cell with a composite SFM-GDC fuel electrode exhibits a linear degradation trend with a minimal increase of 0.016 mV h^{-1}. Ni-GDC electrode-containing ESCs have shown a degradation rate of 0.499 mV h^{-1} in 50% H_2O + 50% H_2, at 900 °C at −0.5 A cm^{-2}.[74] GDC is a mixed ionic and electronic conductor and has been used as a fuel electrode material in ESCs as well. In 50% H_2O + 50% H_2 at 900 °C and −0.5 A cm^{-2}, the cell composed of GDC/8YSZ/GDC/LSCF has exhibited a degradation of 0.112 mV h^{-1}. Fuel Electrode-Supported Cells (FESCs), on the other hand, have been extensively studied in the literature regarding their degradation behavior. Degradation rates of 0.030 mV h^{-1} (ref. 89) to 0.370 mV h^{-1} (ref. 39) have been observed for Ni cermet-supported single cells and 0.024 mV h^{-1},[92] 0.040 mV h^{-1} (ref. 13) to 0.190 mV h^{-1} (ref. 90) for FESC stacks.

Previous studies have characterized SFM fuel electrode materials in humidified atmospheres of steam and co-electrolysis. However, the authors reported degradation measurements only up to 100 h measurement time. The symmetrical SFM/GDC/YbScSZ/GDC/SFM cells with $Sr_2Fe_{1.5}Mo_{0.5}O_{6-\delta}$ showed good stability at −0.5 A cm^2 for 24 h in 75% H_2O + 25% CO_2, and an ASR increase of only 0.03 Ω cm^2.[29] The data in Fig. 8a show a voltage increase of 0.006 V during the first 24 h, which emphasizes that a longer degradation test of 500 h is necessary to assess the degradation of SFM-based fuel electrodes. Degradation tests of SFM composite fuel electrodes in humidified conditions have been conducted for less than 500 h as well.[30,68,91,92] For instance, symmetrical SFM-SDC/LSGM/SFM-SDC ($Sr_2Fe_{1.5}Mo_{0.5}O_{6-\delta}$-$Sm_{0.2}Ce_{0.8}O_{1.9}$) cell tested at −0.12 A
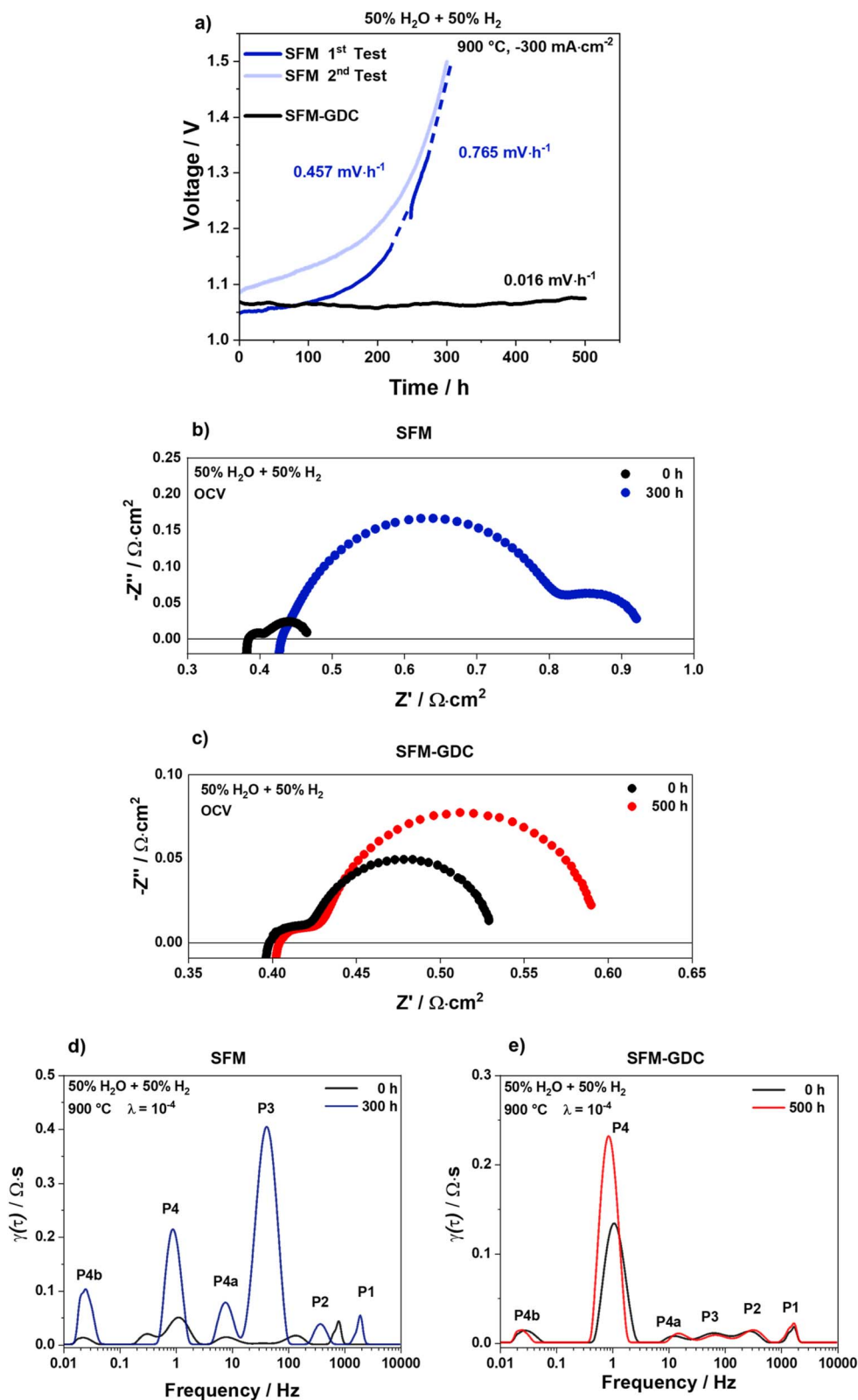
Fig. 8 (a) Long-term stability test of single cells with SFM/GDC/8YSZ/GDC/LSCF and the composite SFM-GDC/GDC/8YSZ/GDC/LSCF in 50% H_2O + 50% H_2 fuel gas composition under constant -0.3 A cm^{-2} current load at 900 °C for up to 500 h. Comparison of (b and c) the Nyquist plots and (d and e) the corresponding DRT spectra recorded before and after the durability test.

cm^2 and 800 °C for 100 h exhibited degradation of 0.130 mV h^{-1}. Similar results were obtained in H_2O/CO_2 co-electrolysis atmosphere at 850 °C, 1.1 V for 100 h.[68] Further characterization was conducted on Ni-doped SFM electrode containing single cells, i.e. $Sr_2Fe_{1.3}Ni_{0.2}Mo_{0.5}O_6$-SDC/LCO/LSGM/SDC-LSCF in 42% H_2O + 58% H_2 for 60 h under a current load of −0.3 A cm^{-2}, and the authors concluded that this electrode is stable at high temperatures and high humidity.[30]

For further detailed degradation analysis, impedance spectra were recorded before and after the degradation test. The spectra in addition to the DRT analysis are displayed in Fig. 8b–e and were measured at OCV and 900 °C with a fuel gas composition of 50% H_2O + 50% H_2. The individual process resistances of the fitted spectra are given in Table 3. The total resistance (ASR) for the cell based on an SFM fuel electrode after around 300 h increases from 468 mΩ cm^2 to 959 mΩ cm^2. In comparison, over 500 h of measurement, the ASR increases only 64 mΩ cm^2 from 532 mΩ cm^2 to 596 mΩ cm^2 for the SFM-GDC fuel electrode. It can be discerned from the fitted results and the impedance spectra, the contribution of the ohmic resistance R_Ω to the ASR increase over the measurement time is minimal in comparison to the polarization resistance R_P. For the SFM cell, the increase in ohmic resistance accounted for around 8.8% of the ASR change, which is in the range of 9.4% found for the SFM-GDC cell. On the other hand, a large increase in the R_P, i.e. 448 mΩ cm^2 is observed for the severely degraded SFM cell. This is mainly due to an increase in the process resistances R_{RQ2}, R_{RQ3}, and R_{RQ4}. The resistance values for the SFM-GDC fuel electrode (Table 3) correspond to the lower voltage increase and smaller changes in the Nyquist plot (Fig. 8c). In addition to the small ohmic resistance increase of 6 mΩ cm^2, the polarization resistance increases by 58 mΩ cm^2 due to an increase in R_{RQ4}. The DRT analysis is in support of these results and shows a shift of R_{RQ1} to higher frequencies without an increase in P1. The resistances P2, P3, and P4 for SFM cell as well as P4 for SFM-GDC cell, however, display an increase. Thus, the performance loss after the degradation test can be mainly attributed to the mid-to low-frequency process P3 and P4 linked with the SFM fuel electrode as well as to a lesser part to the oxygen electrodes associated with the high-to mid-frequency processes. The degradation observed for SFM-GDC is attributed to the

process P4 as well, while P1, P2, and P3 remain relatively constant.

3.3.2. Post-test SEM analysis. After the long-term stability measurements under constant load, the tested cells as well as as-prepared single cells were investigated through SEM-EDX analysis. The samples were embedded in epoxy resin, polished and Au sputtered before analysis. The SEM-EDX analyses of as-prepared and post-test cell cross-sections for SFM and SFM-GDC electrodes are shown in Fig. 9a and b. For all cells, the electrolyte is crack-free, and no delamination of the electrodes is observed. The composite SFM-GDC electrode exhibits an even distribution of GDC particles in the SFM electrode microstructure before and after the 500 h long-term stability test in 50% H_2O + 50% H_2 at 900 °C and constant −0.3 A cm^{-2}. Very slight Sr segregation of the SFM-GDC composite structure through the GDC barrier layer to the GDC/8YSZ interface is observed. This can be connected to an insufficiently dense GDC layer. In addition, a striking structural instability of the SFM fuel electrode is observed through the evolution of a dense layer at the SFM/GDC interface. The EDX analysis in Fig. 9a reveals that the formed phase consists pre-dominantly of Sr and Fe. To the author's knowledge, this phase formation at the GDC barrier layer/SFM fuel electrode interface after long-term operation in steam electrolysis has not been reported in the literature up to now.

Sr segregation has been mainly reported for Sr-containing oxygen electrodes after degradation testing and has been linked to the material's stoichiometry, ion mobility as well as operating conditions (temperature, polarization). Strontium-doped Lanthanum Manganite (LSM) exhibits high cation mobility and inter-diffusion under a high anodic current (−1.5 A cm^{-2} at 750 °C).[93] Similar observations have been made for Sr-perovskite materials like $SrTiO_3$ (STO),[94] $SrTi_{1-x}Fe_xO_3$ (STF),[95] and $Sr_2Fe_{1.5}Mo_{0.5}O_{6-\delta}$ (SFM15).[96] The origin of the segregation mechanism in Sr-containing fuel electrode perovskite materials will have to be further investigated in the future. A starting point could be the structural instability of the perovskite material under operating conditions as described above. This could in turn lead to higher cation mobility in addition to a change in stoichiometry and oxygen vacancies. The SEM-EDX of SFM-GDC also shown in Fig. 9 displays no phase formation at the electrode/GDC interface after 500 h in steam electrolysis conditions. The composite SFM-GDC fuel electrode exhibits, therefore, superior chemical stability in humidified conditions as also shown in the cell voltage vs. time curve (Fig. 8).

Further SEM-EDX analyses for the LSCF oxygen electrode are displayed in Fig. S11 for the as-prepared and operated cells. Although a GDC barrier layer was deposited on the 8YSZ electrolyte, the volatile SrO diffused through the pores or along the grain boundaries of the GDC layer to the GDC/8YSZ interface and formed an electronically insulating $SrZrO_3$ phase. The amount of formed $SrZrO_3$ indicates the degree of Sr segregation at the GDC/YSZ interface and it can be seen from Fig. S11 that the extent of Sr segregation increases after the long-term test. This mechanism of Sr-segregation in LSCF electrodes has been widely discussed.[16,17,97–107] The formation of the insulating $SrZrO_3$ phase already occurs during the sintering process of the LSCF electrode

Table 3 Individual process resistances before and after the degradation tests taken from ECM fitting before and after the degradation test in 50% H_2O + 50% H_2 at 900 °C and constant −0.3 A cm^{-2} current load for up to 500 h

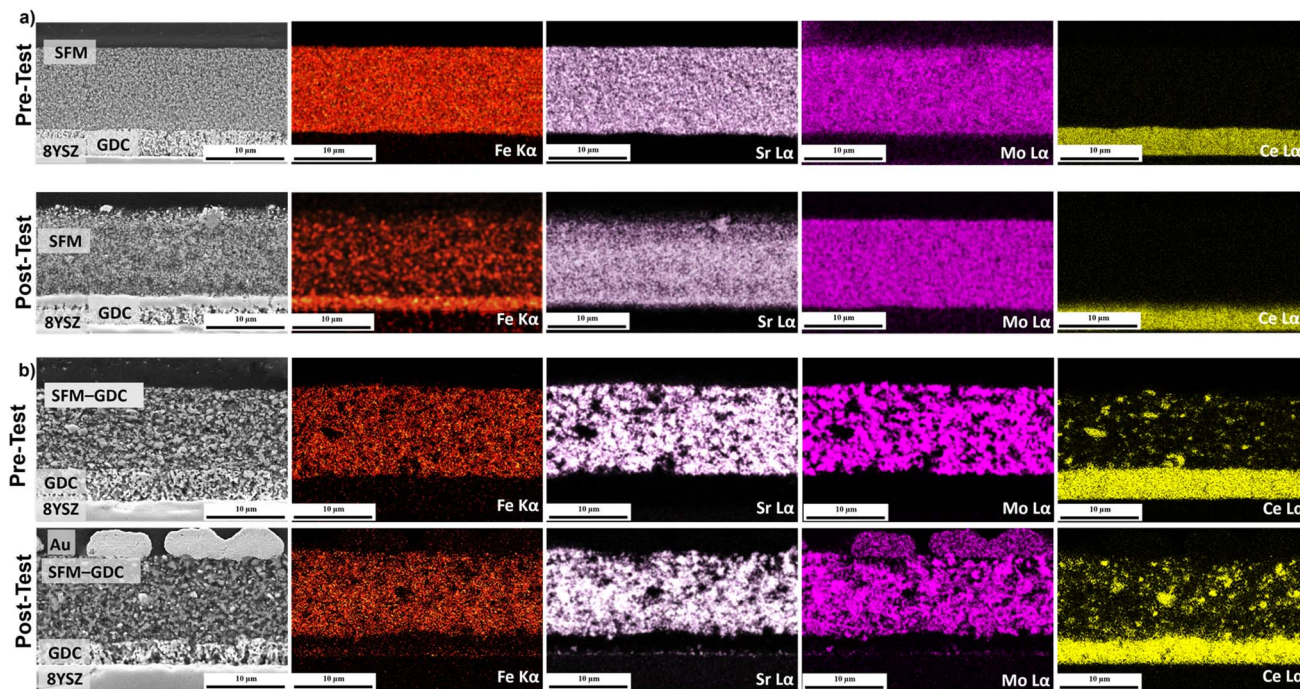| Time/h	R_Ω	R_{RQ1}	R_{RQ2}	R_{RQ3}	R_{RQ4}	R_P	ASR
Resistances/mΩ cm^2							
SFM							
0	382	6	19	9	52	86	468
300	425	55	207	125	147	534	959
SFM-GDC							
0	395	3	10	18	106	137	532
500	401	5	11	17	162	195	596

Fig. 9 Cross-sectional SEM-EDX mapping of the fuel electrode side for Sr (Lα, 13.89 keV), Fe (Κα, 6.40 keV), Mo (Lα, 17.14 keV), Ce (Lα, 33.90 keV) lines of as-prepare and tested (a) SFM and (b) SFM-GDC single cells operating in steam electrolysis at -0.3 A cm^{-2} up to 500 h.

and deteriorates during the electrolysis operation of the cell.[13,108] The Sr-loss from the electrode leads to reduced ionic and electronic conductivity, hindered O$^-$ ion flux, loss of active Triple or Double Phase Boundary (TPB or DPB) length of the electrode, and consequently cell performance loss[106] as indicated by increased polarization resistance (R_p)[104,109] as well as ohmic resistance.[97]

4. Conclusion

In this study, the electrocatalytic active SFM and composite SFM-GDC fuel electrode materials were characterized for SOECs. The phase conversion at high temperatures in reducing conditions was visualized using XRD and *in situ* TEM analyses. The reduced sample showed phase formation of mixed Ruddlesden–Popper, simple cubic perovskite Sr(Fe$_{0.8}$Mo$_{0.2}$)O$_3$, double perovskite Sr$_2$(Fe$_{1.33}$Mo$_{0.66}$)O$_{5.88}$, and Fe nanoparticle exsolution after reduction. The performance and long-term stability of electrolyte-supported single cells with SFM and composite SFM-GDC fuel electrodes were characterized in humidified conditions. For the SFM cell, current densities of -1.26 A cm^{-2} were achieved for steam electrolysis and -1.27 A cm^{-2} in co-electrolysis conditions at 1.5 V and 900 °C. With SFM-GDC cell, current densities of -1.24 A cm^{-2} and -1.27 A cm^{-2} at 1.5 V and 900 °C were achieved for steam and electrolysis respectively. Irrespective of measurement conditions, the cells with SFM-based fuel electrodes outperformed the state-of-the-art Ni-8YSZ fuel electrode produced with the same cell design. However, the Ni-GDC fuel-electrode containing single cells exhibited slightly higher current densities under both electrolysis conditions. Durability tests at a constant load of

-0.3 A cm^{-2} were performed at 900 °C in steam electrolysis conditions for up to 500 h. The cell voltage showed an exponential increase for SFM after 100 h, while the SFM-GDC-containing cell exhibited a linear degradation trend. The impedance spectra taken before and after the durability tests underlined that the cell with an SFM electrode shows a higher degradation corresponding to a severe increase in ohmic and polarization resistance. For SFM-GDC cells, on the other hand, the resistance increase is negligible.

The post-test analysis revealed Sr-segregation at the GDC/YSZ interface towards the oxygen electrode side for both SFM and SFM-GDC cells. However, a striking structural instability of the SFM fuel electrode and subsequent formation of a dense layer at the SFM/GDC interface was observed. The EDX analysis revealed that the formed phase consists pre-dominantly of Sr and Fe. However, interestingly, such interphase formation was not observed for SFM-GDC cells. Therefore, the phase instability of SFM is the most significant reason for the severe degradation of SFM cells.

Conflicts of interest

There are no conflicts to declare.

Data availability

The original data of this manuscript are available and can be accessed using the following link. **https://data.fz-juelich.de/privateurl.xhtml?token=e56a562c-c1d9-4325-988b-90eee4b4ba5c.**

References

1 S. E. Wolf, F. E. Winterhalder, V. Vibhu, L. G. J. de Haart, O. Guillon, R.-A. Eichel and N. H. Menzler, Solid oxide electrolysis cells – current material development and industrial application, *J. Mater. Chem. A*, 2023, **11**, 17977–18028.

2 L. Dittrich, M. Nohl, E. E. Jaekel, S. Foit, L. G. J. de Haart and R.-A. Eichel, High-Temperature Co-Electrolysis: A Versatile Method to Sustainably Produce Tailored Syngas Compositions, *J. Electrochem. Soc.*, 2019, **166**, F971–F975.

3 Y. Zheng, J. Wang, B. Yu, W. Zhang, J. Chen, J. Qiao and J. Zhang, A review of high temperature co-electrolysis of H2O and CO2 to produce sustainable fuels using solid oxide electrolysis cells (SOECs): advanced materials and technology, *Chem. Soc. Rev.*, 2017, **46**, 1427–1463.

4 M. E. Dry, The Fischer–Tropsch process: 1950–2000, *Catal. Today*, 2002, **71**, 227–241.

5 S. D. Ebbesen, S. H. Jensen, A. Hauch and M. B. Mogensen, High temperature electrolysis in alkaline cells, solid proton conducting cells, and solid oxide cells, *Chem. Rev.*, 2014, **114**, 10697–10734.

6 J. Artz, T. E. Müller, K. Thenert, J. Kleinekorte, R. Meys, A. Sternberg, A. Bardow and W. Leitner, Sustainable Conversion of Carbon Dioxide: An Integrated Review of Catalysis and Life Cycle Assessment, *Chem. Rev.*, 2018, **118**, 434–504.

7 S. D. Ebbesen, C. Graves and M. Mogensen, Production of Synthetic Fuels by Co-Electrolysis of Steam and Carbon Dioxide, *Int. J. Green Energy*, 2009, **6**, 646–660.

8 C. Graves, S. D. Ebbesen, M. Mogensen and K. S. Lackner, Sustainable hydrocarbon fuels by recycling CO 2 and H 2 O with renewable or nuclear energy, *Renewable Sustainable Energy Rev.*, 2011, **15**, 1–23.

9 S.-W. Kim, H. Kim, K. J. Yoon, J.-H. Lee, B.-K. Kim, W. Choi, J.-H. Lee and J. Hong, Reactions and mass transport in high temperature co-electrolysis of steam/CO2 mixtures for syngas production, *J. Power Sources*, 2015, **280**, 630–639.

10 M. Bjerg Mogensen, *Thermodynamics of high temperature H2O and CO2 electrolysis*, 2020, DOI: **10.6084/m9.figshare.12652322.v1**.

11 R. Küngas, Review—Electrochemical CO 2 Reduction for CO Production: Comparison of Low- and High-Temperature Electrolysis Technologies, *J. Electrochem. Soc.*, 2020, **167**, 44508.

12 M. Trini, A. Hauch, S. de Angelis, X. Tong, P. V. Hendriksen and M. Chen, Comparison of microstructural evolution of fuel electrodes in solid oxide fuel cells and electrolysis cells, *J. Power Sources*, 2020, **450**, 227599.

13 F. Tietz, D. Sebold, A. Brisse and J. Schefold, Degradation phenomena in a solid oxide electrolysis cell after 9000 h of operation, *J. Power Sources*, 2013, **223**, 129–135.

14 M. Hubert, J. Laurencin, P. Cloetens, B. Morel, D. Montinaro and F. Lefebvre-Joud, Impact of Nickel agglomeration on Solid Oxide Cell operated in fuel cell and electrolysis modes, *J. Power Sources*, 2018, **397**, 240–251.

15 P. S. Jørgensen and J. R. Bowen, Determination of Three Dimensional Microstructure Parameters from a Solid Oxide Ni/YSZ Electrode after Electrolysis Operation, *ECS Trans.*, 2011, **35**, 1655–1660.

16 D. The, S. Grieshammer, M. Schroeder, M. Martin, M. Al Daroukh, F. Tietz, J. Schefold and A. Brisse, Microstructural comparison of solid oxide electrolyser cells operated for 6100 h and 9000 h, *J. Power Sources*, 2015, **275**, 901–911.

17 G. Rinaldi, S. Diethelm, E. Oveisi, P. Burdet, J. van Herle, D. Montinaro, Q. Fu and A. Brisse, Post-test Analysis on a Solid Oxide Cell Stack Operated for 10,700 Hours in Steam Electrolysis Mode, *Fuel Cells*, 2017, **17**, 541–549.

18 Q. Fang, C. E. Frey, N. H. Menzler and L. Blum, Electrochemical Performance and Preliminary Post-Mortem Analysis of a Solid Oxide Cell Stack with 20,000 h of Operation, *J. Electrochem. Soc.*, 2018, **165**, F38–F45.

19 M. P. Hoerlein, M. Riegraf, R. Costa, G. Schiller and K. A. Friedrich, A parameter study of solid oxide electrolysis cell degradation: Microstructural changes of the fuel electrode, *Electrochim. Acta*, 2018, **276**, 162–175.

20 M. Trini, P. S. Jørgensen, A. Hauch, J. J. Bentzen, P. V. Hendriksen and M. Chen, 3D Microstructural Characterization of Ni/YSZ Electrodes Exposed to 1 Year of Electrolysis Testing, *J. Electrochem. Soc.*, 2019, **166**, F158–F167.

21 E. Lay-Grindler, J. Laurencin, J. Villanova, P. Cloetens, P. Bleuet, A. Mansuy, J. Mougin and G. Delette, Degradation study by 3D reconstruction of a nickel–yttria stabilized zirconia cathode after high temperature steam electrolysis operation, *J. Power Sources*, 2014, **269**, 927–936.

22 M. Keane, H. Fan, M. Han and P. Singh, Role of initial microstructure on nickel-YSZ cathode degradation in solid oxide electrolysis cells, *Int. J. Hydrogen Energy*, 2014, **39**, 18718–18726.

23 M. B. Mogensen, A. Hauch, X. Sun, M. Chen, Y. Tao, S. D. Ebbesen, K. V. Hansen and P. V. Hendriksen, Relation Between Ni Particle Shape Change and Ni Migration in Ni-YSZ Electrodes - a Hypothesis, *Fuel Cells*, 2017, **17**, 434–441.

24 R. Xing, Y. Wang, S. Liu and C. Jin, Preparation and characterization of La0.75Sr0.25Cr0.5Mn0.5O3−δ-yttria stabilized zirconia cathode supported solid oxide electrolysis cells for hydrogen generation, *J. Power Sources*, 2012, **208**, 276–281.

25 B. Ge, J. Sheng, Y. Zhuang, J. Ma, Z. Yang, C. Li and S. Peng, Effects of the atmosphere and Mn doping on the electrical properties of Sr2Fe1−xMnxNbO6 and their mechanisms, *Mater. Res. Express*, 2020, **7**.

26 Q. Qin, K. Xie, H. Wei, W. Qi, J. Cui and Y. Wu, Demonstration of efficient electrochemical biogas reforming in a solid oxide electrolyser with titanate cathode, *RSC Adv.*, 2014, **4**, 38474–38483.

27 J. Zhou, L. Xu, C. Ding, C. Wei and Z. Tao, Layered perovskite (PrBa)0.95(Fe0.9Mo0.1)2O5+δ as electrode materials for high-performing symmetrical solid oxide electrolysis cells, *Mater. Lett.*, 2019, **257**, 126758.

28 G. Xiao, Q. Liu, F. Zhao, L. Zhang, C. Xia and F. Chen, Sr2Fe1.5Mo0.5O6 as Cathodes for Intermediate-Temperature Solid Oxide Fuel Cells with La0.8Sr0.2Ga0.87Mg0.13O3 Electrolyte, *J. Electrochem. Soc.*, 2011, **158**, B455.

29 L. Bernadet, C. Moncasi, M. Torrell and A. Tarancón, High-performing electrolyte-supported symmetrical solid oxide electrolysis cells operating under steam electrolysis and co-electrolysis modes, *Int. J. Hydrog. Energy*, 2020, **45**, 14208–14217.

30 Y. Wang, T. Liu, M. Li, C. Xia, B. Zhou and F. Chen, Exsolved Fe–Ni nano-particles from Sr2Fe1.3Ni0.2Mo0.5O6 perovskite oxide as a cathode for solid oxide steam electrolysis cells, *J. Mater. Chem. A*, 2016, **4**, 14163–14169.

31 Q. Liu, D. E. Bugaris, G. Xiao, M. Chmara, S. Ma, H.-C. zur Loye, M. D. Amiridis and F. Chen, Sr2Fe1.5Mo0.5O6−δ as a regenerative anode for solid oxide fuel cells, *J. Power Sources*, 2011, **196**, 9148–9153.

32 Y. Guo, T. Guo, S. Zhou, Y. Wu, H. Chen, X. Ou and Y. Ling, Characterization of Sr2Fe1.5Mo0.5O6-δ -Gd0.1Ce0.9O1.95 symmetrical electrode for reversible solid oxide cells, *Ceram. Int.*, 2019, **45**, 10969–10975.

33 J. Gao, X. Meng, T. Luo, H. Wu and Z. Zhan, Symmetrical solid oxide fuel cells fabricated by phase inversion tape casting with impregnated SrFe0.75Mo0.25O3-δ (SFMO) electrodes, *Int. J. Hydrogen Energy*, 2017, **42**, 18499–18503.

34 S. E. Wolf, Electrochemical Analysis and Development of Novel Electrode Materials for High-Temperature Electrolysis, PhD thesis, RWTH Aachen University, 2025, DOI: 10.18154/RWTH-2025-01207.

35 V. Vibhu, I. C. Vinke, F. Zaravelis, S. G. Neophytides, D. K. Niakolas, R.-A. Eichel and L. G. J. de Haart, Performance and Degradation of Electrolyte-Supported Single Cell Composed of Mo-Au-Ni/GDC Fuel Electrode and LSCF Oxygen Electrode during High Temperature Steam Electrolysis, *Energies*, 2022, **15**, 2726.

36 A. A. Coelho, TOPAS and TOPAS-Academic : an optimization program integrating computer algebra and crystallographic objects written in C++, *J. Appl. Crystallogr.*, 2018, **51**, 210–218.

37 Coelho Software, *TOPAS-academic Version 6 (Computer Software)*, Bruker AXS, Karlsruhe, Germany.

38 V. Vibhu, S. Yildiz, I. C. Vinke, R.-A. Eichel, J.-M. Bassat and L. G. J. de Haart, High Performance LSC Infiltrated LSCF Oxygen Electrode for High Temperature Steam Electrolysis Application, *J. Electrochem. Soc.*, 2019, **166**, F102–F108.

39 S. E. Wolf, V. Vibhu, E. Tröster, I. C. Vinke, R.-A. Eichel and L. G. J. de Haart, Steam Electrolysis *vs.* Co-Electrolysis: Mechanistic Studies of Long-Term Solid Oxide Electrolysis Cells, *Energies*, 2022, **15**, 5449.

40 S. E. Wolf, L. Dittrich, M. Nohl, T. Duyster, I. C. Vinke, R.-A. Eichel and L. G. J. de Haart, Boundary Investigation of High-Temperature Co-Electrolysis towards Direct CO2 Electrolysis, *J. Electrochem. Soc.*, 2022, **169**, 34531.

41 Q. Liu, X. Dong, G. Xiao, F. Zhao and F. Chen, A novel electrode material for symmetrical SOFCs, *Adv. Mater.*, 2010, **22**, 5478–5482.

42 G. Miao, C. Yuan, T. Chen, Y. Zhou, W. Zhan and S. Wang, Sr2Fe1+xMo1−xO6−δ as anode material of cathode–supported solid oxide fuel cells, *Int. J. Hydrogen Energy*, 2016, **41**, 1104–1111.

43 J. Rager, M. Zipperle, A. Sharma and J. L. MacManus-Driscoll, Oxygen Stoichiometry in Sr2FeMoO6, the Determination of Fe and Mo Valence States, and the Chemical Phase Diagram of SrO-Fe3O4-MoO3, *J. Am. Ceram. Soc.*, 2004, **87**, 1330–1335.

44 A. B. Muñoz-García, D. E. Bugaris, M. Pavone, J. P. Hodges, A. Huq, F. Chen, H.-C. zur Loye and E. A. Carter, Unveiling structure-property relationships in Sr2Fe(1.5)Mo(0.5)O(6-δ), an electrode material for symmetric solid oxide fuel cells, *J. Am. Chem. Soc.*, 2012, **134**, 6826–6833.

45 O. A. Savinskaya, A. P. Nemudry, A. N. Nadeev, S. V. Tsybulya and N. Z. Lyakhov, High-temperature study of SrFe1 − x Mo x O3−z perovskites, *Bull. Russ. Acad. Sci.: Phys.*, 2010, **74**, 1053–1054.

46 O. Savinskaya and A. P. Nemudry, Oxygen transport properties of nanostructured SrFe1 − x Mo x O2.5 + 3/2x (0 < x < 0.1) perovskites, *J. Solid State Electrochem.*, 2011, **15**, 269–275.

47 G. M. Veith, M. Greenblatt, M. Croft, K. V. Ramanujachary, J. Hattrick-Simpers, S. E. Lofland and I. Nowik, Synthesis and Characterization of Sr3FeMoO6.88 : An Oxygen-Deficient 2D Analogue of the Double Perovskite Sr2FeMoO6, *Chem. Mater.*, 2005, **17**, 2562–2567.

48 F. Sher, A. J. Williams, A. Venimadhev, M. G. Blamire and J. P. Attfield, Synthesis, Structure, and Properties of Two

New Ruddlesden−Popper Phase Analogues of SFMO (Sr 2 FeMoO 6), *Chem. Mater.*, 2005, **17**, 1792–1796.

49 B. K. Maji, H. Jena, R. Asuvathraman and K. G. Kutty, Electrical conductivity and thermal expansion behavior of MMoO4 (M=Ca, Sr and Ba), *J. Alloys Compd.*, 2015, **640**, 475–479.

50 B. He, L. Zhao, S. Song, T. Liu, F. Chen and C. Xia, Sr 2 Fe 1.5 Mo 0.5 O 6−δ - Sm 0.2 Ce 0.8 O 1.9 Composite Anodes for Intermediate-Temperature Solid Oxide Fuel Cells, *J. Electrochem. Soc.*, 2012, **159**, B619–B626.

51 B. Steele, Appraisal of Ce1−yGdyO2−y/2 electrolytes for IT-SOFC operation at 500°C, *Solid State Ionics*, 2000, **129**, 95–110.

52 A. J. Jacobson, Materials for Solid Oxide Fuel Cells, *Chem. Mater.*, 2010, **22**, 660–674.

53 A. Nenning, M. Holzmann, J. Fleig and A. K. Opitz, Excellent kinetics of single-phase Gd-doped ceria fuel electrodes in solid oxide cells, *Mater. Adv.*, 2021, **2**, 5422–5431.

54 J. Paier, C. Penschke and J. Sauer, Oxygen defects and surface chemistry of ceria: quantum chemical studies compared to experiment, *Chem. Rev.*, 2013, **113**, 3949–3985.

55 G. Kim, G. Corre, J. T. S. Irvine, J. M. Vohs and R. J. Gorte, Engineering Composite Oxide SOFC Anodes for Efficient Oxidation of Methane, *Electrochem. Solid-State Lett.*, 2008, **11**, B16.

56 Y.-H. Huang, R. I. Dass, J. C. Denyszyn and J. B. Goodenough, Synthesis and Characterization of Sr [sub 2]MgMoO[sub 6−δ], *J. Electrochem. Soc.*, 2006, **153**, A1266.

57 B. Ge, J. T. Ma, D. Ai, C. Deng, X. Lin and J. Xu, Sr2FeNbO6 Applied in Solid Oxide Electrolysis Cell as the Hydrogen Electrode: Kinetic Studies by Comparison with Ni-YSZ, *Electrochim. Acta*, 2015, **151**, 437–446.

58 Y. Jiang, Y. Yang, C. Xia and H. J. M. Bouwmeester, Sr 2 Fe 1.4 Mn 0.1 Mo 0.5 O 6−δ perovskite cathode for highly efficient CO 2 electrolysis, *J. Mater. Chem. A*, 2019, **7**, 22939–22949.

59 Z. Du, H. Zhao, S. Yi, Q. Xia, Y. Gong, Y. Zhang, X. Cheng, Y. Li, L. Gu and K. Świerczek, High-Performance Anode Material Sr2FeMo0.65Ni0.35O6-δ with *In Situ* Exsolved Nanoparticle Catalyst, *ACS Nano*, 2016, **10**, 8660–8669.

60 X. Xi, Y. Fan, J. Zhang, J.-L. Luo and X.-Z. Fu, In-situ Construction of Hetero-structured Perovskite Composites with Exsolved Fe and Cu Metallic Nanoparticles as Efficient CO2 Reduction Electrocatalyst for High Performance Solid Oxide Electrolysis Cells, *J. Mater. Chem. A*, 2022, **10**(5), 2509–2518.

61 P. Arnoldy, J. C. M. de Jonge and J. A. Moulijn, Temperature-programed reduction of molybdenum(VI) oxide and molybdenum(IV) oxide, *J. Phys. Chem.*, 1985, **89**, 4517–4526.

62 P. K. Chakraborty, S. E. Wolf, G. Ummethala, A. Meise, T. Mehlkoph, J. Park, M. Heggen, A. H. Tavabi, V. Vibhu, A. Karl, E. Jodat, L. de Haart, R. E. Dunin-Borowski, S. Basak and R.-A. Eichel, Unveiling the exsolution mechanisms and investigation of the catalytic processes of Sr2FeMo0.65Ni0.35O6-δ using *in situ* transmission electron microscopy, *Nano Today*, 2025, **61**, 102649.

63 P. Qiu, X. Yang, W. Wang, T. Wei, Y. Lu, J. Lin, Z. Yuan, L. Jia, J. Li and F. Chen, Redox-Reversible Electrode Material for Direct Hydrocarbon Solid Oxide Fuel Cells, *ACS Appl. Mater. Interfaces*, 2020, **12**, 13988–13995.

64 F. Song, K. Schenk and X. Hu, A nanoporous oxygen evolution catalyst synthesized by selective electrochemical etching of perovskite hydroxide CoSn(OH) 6 nanocubes, *Energy Environ. Sci.*, 2016, **9**, 473–477.

65 M. Shao, B. H. Smith, S. Guerrero, L. Protsailo, D. Su, K. Kaneko, J. H. Odell, M. P. Humbert, K. Sasaki, J. Marzullo and R. M. Darling, Core-shell catalysts consisting of nanoporous cores for oxygen reduction reaction, *Phys. Chem. Chem. Phys.*, 2013, **15**, 15078–15090.

66 X. Xi, X.-W. Wang, Y. Fan, Q. Wang, Y. Lu, J. Li, L. Shao, J.-L. Luo and X.-Z. Fu, Efficient bifunctional electrocatalysts for solid oxide cells based on the structural evolution of perovskites with abundant defects and exsolved CoFe nanoparticles, *J. Power Sources*, 2021, **482**, 228981.

67 Y. Li, B. Hu, C. Xia, W. Q. Xu, J. P. Lemmon and F. Chen, A novel fuel electrode enabling direct CO 2 electrolysis with excellent and stable cell performance, *J. Mater. Chem. A*, 2017, **5**, 20833–20842.

68 S. Hou and K. Xie, Enhancing the performance of high-temperature H2O/CO2 co-electrolysis process on the solid oxide Sr2Fe1.6Mo0.5O6-δ-SDC/LSGM/Sr2Fe1.5Mo0.5O6-δ-SDC cell, *Electrochim. Acta*, 2019, **301**, 63–68.

69 F. Tietz, Thermal expansion of SOFC materials, *Ionics*, 1999, **5**, 129–139.

70 F. Tietz, I. A. Raj, M. Zahid, A. Mai and D. Stöver, Survey of the quasi-ternary system La0.8Sr0.2MnO3–La0.8Sr0.2CoO3–La0.8Sr0.2FeO3, *Prog. Solid State Chem.*, 2007, **35**, 539–543.

71 K. Sick, N. Grigorev, N. H. Menzler and O. Guillon, in *Proceeding of the 42nd International Conference on Advanced Ceramics and Composites*, ed. J. Salem, D. Koch, P. Mechnich, M. Kusnezoff, N. Bansal, J. LaSalvia, P. Balaya, Z. Fu and T. Ohji, John Wiley & Sons, Inc, Hoboken, NJ, USA, 2019, pp. 99–111.

72 Z. Wang, Y. Tian and Y. Li, Direct CH4 fuel cell using Sr2FeMoO6 as an anode material, *J. Power Sources*, 2011, **196**, 6104–6109.

73 I. D. Unachukwu, V. Vibhu, J. Uecker, I. C. Vinke, R.-A. Eichel and L. G. J. de Haart, Comparison of the Electrochemical and Degradation Behaviour of Ni-YSZ and Ni-GDC Electrodes Under Steam, Co- and CO 2 Electrolysis, *ECS Trans.*, 2023, **111**, 1445–1452.

74 I. D. Unachukwu, V. Vibhu, I. C. Vinke, R.-A. Eichel and L. G. J. de Haart, Electrochemical and degradation behaviour of single cells comprising Ni-GDC fuel electrode under high temperature steam- and co-electrolysis conditions, *J. Power Sources*, 2023, **556**, 232436.

75 J. Uecker, I. D. Unachukwu, V. Vibhu, I. C. Vinke, R.-A. Eichel and L. G. J. de Haart, Performance, electrochemical process analysis and degradation of gadolinium doped ceria as fuel electrode material for

solid oxide electrolysis cells, *Electrochim. Acta*, 2023, **452**, 142320.

76 F. Kundracik, M. Hartmanová, J. Müllerová, M. Jergel, I. Kostič and R. Tucoulou, Ohmic resistance of thin yttria stabilized zirconia film and electrode–electrolyte contact area, *J. Mater. Sci. Eng. B*, 2001, **84**, 167–175.

77 S. D. Ebbesen and M. Mogensen, Electrolysis of carbon dioxide in Solid Oxide Electrolysis Cells, *J. Power Sources*, 2009, **193**, 349–358.

78 A. Leonide, V. Sonn, A. Weber and E. Ivers-Tiffée, Evaluation and Modeling of the Cell Resistance in Anode-Supported Solid Oxide Fuel Cells, *J. Electrochem. Soc.*, 2008, **155**, B36.

79 C. Li, Y. Deng, L. Yang, B. Liu, D. Yan, L. Fan, J. Li and L. Jia, An active and stable hydrogen electrode of solid oxide cells with exsolved Fe–Co–Ni nanoparticles from Sr2FeCo0.2Ni0.2Mo0.6O6-δ double-perovskite, *Adv. Powder Mater.*, 2023, **2**, 100133.

80 H. Lv, L. Lin, X. Zhang, D. Gao, Y. Song, Y. Zhou, Q. Liu, G. Wang and X. Bao, In situ exsolved FeNi 3 nanoparticles on nickel doped Sr 2 Fe 1.5 Mo 0.5 O 6−δ perovskite for efficient electrochemical CO 2 reduction reaction, *J. Mater. Chem. A*, 2019, **7**, 11967–11975.

81 X. Xi, J. Liu, W. Luo, Y. Fan, J. Zhang, J.-L. Luo and X.-Z. Fu, Unraveling the Enhanced Kinetics of Sr 2 Fe 1+x Mo 1-x O 6-δ Electrocatalysts for High-Performance Solid Oxide Cells, *Adv. Energy Mater.*, 2021, **11**, 2102845.

82 S. Primdahl, Mixed conductor anodes: Ni as electrocatalyst for hydrogen conversion, *Solid State Ionics*, 2002, **152–153**, 597–608.

83 Z. A. Feng, F. El Gabaly, X. Ye, Z.-X. Shen and W. C. Chueh, Fast vacancy-mediated oxygen ion incorporation across the ceria-gas electrochemical interface, *Nat. Commun.*, 2014, **5**, 4374.

84 M. Riegraf, R. Costa, G. Schiller, K. A. Friedrich, S. Dierickx and A. Weber, Electrochemical Impedance Analysis of Symmetrical Ni/Gadolinium-Doped Ceria (CGO10) Electrodes in Electrolyte-Supported Solid Oxide Cells, *J. Electrochem. Soc.*, 2019, **166**, F865–F872.

85 P. Caliandro, A. Nakajo, S. Diethelm and J. van Herle, Model-assisted identification of solid oxide cell elementary processes by electrochemical impedance spectroscopy measurements, *J. Power Sources*, 2019, **436**, 226838.

86 D. Papurello, D. Menichini and A. Lanzini, Distributed relaxation times technique for the determination of fuel cell losses with an equivalent circuit model to identify physicochemical processes, *Electrochim. Acta*, 2017, **258**, 98–109.

87 D. G. Goodwin, H. Zhu, A. M. Colclasure and R. J. Kee, Modeling Electrochemical Oxidation of Hydrogen on Ni–YSZ Pattern Anodes, *J. Electrochem. Soc.*, 2009, **156**, B1004.

88 S. Primdahl and Y. L. Liu, Ni Catalyst for Hydrogen Conversion in Gadolinia-Doped Ceria Anodes for Solid Oxide Fuel Cells, *J. Electrochem. Soc.*, 2002, **149**, A1466.

89 A. Padinjarethil and A. Hagen, The Identification of Degradation Parameters in SOC Under Load and OCV Aging Approaches, *ECS Adv.*, 2023, **2**, 24503.

90 S. D. Ebbesen, J. Høgh, K. A. Nielsen, J. U. Nielsen and M. Mogensen, Durable SOC stacks for production of hydrogen and synthesis gas by high temperature electrolysis, *Int. J. Hydrogen Energy*, 2011, **36**, 7363–7373.

91 Y. Yang, Z. Yang, Y. Chen, F. Chen and S. Peng, A Promising Composite Anode for Solid Oxide Fuel Cells: Sr 2 FeMo 0.65 Ni 0.35 O 6-δ -Gd 0.1 Ce 0.9 O 2-δ, *J. Electrochem. Soc.*, 2019, **166**, F109–F113.

92 Y. Wang, T. Liu, S. Fang and F. Chen, Syngas production on a symmetrical solid oxide H2O/CO2 co-electrolysis cell with Sr2Fe1.5Mo0.5O6–Sm0.2Ce0.8O1.9 electrodes, *J. Power Sources*, 2016, **305**, 240–248.

93 J. Kim, H.-I. Ji, H. P. Dasari, D. Shin, H. Song, J.-H. Lee, B.-K. Kim, H.-J. Je, H.-W. Lee and K. J. Yoon, Degradation mechanism of electrolyte and air electrode in solid oxide electrolysis cells operating at high polarization, *Int. J. Hydrogen Energy*, 2013, **38**, 1225–1235.

94 K. Szot, M. Pawelczyk, J. Herion, C. Freiburg, J. Albers, R. Waser, J. Hulliger, J. Kwapulinski and J. Dec, Nature of the surface layer in ABO3-type perovskites at elevated temperatures, *Appl. Phys. A*, 1996, **62**, 335–343.

95 Y. Chen, W. Jung, Z. Cai, J. J. Kim, H. L. Tuller and B. Yildiz, Impact of Sr segregation on the electronic structure and oxygen reduction activity of SrTi1−xFexO3 surfaces, *Energy Environ. Sci.*, 2012, **5**, 7979.

96 H.-Y. Li and P.-C. Su, Applied current on the suppression of strontium segregation in Sr2Fe1.5Mo0.5O6-δ electrode for improved oxygen evolution reaction, *Appl. Mater. Today*, 2023, **31**, 101769.

97 F. Monaco, D. Ferreira-Sanchez, M. Hubert, B. Morel, D. Montinaro, D. Grolimund and J. Laurencin, Oxygen electrode degradation in solid oxide cells operating in electrolysis and fuel cell modes: LSCF destabilization and interdiffusion at the electrode/electrolyte interface, *Int. J. Hydrogen Energy*, 2021, **46**, 31533–31549.

98 H. Tu, Y. Takeda, N. Imanishi and O. Yamamoto, Ln0.4Sr0.6Co0.8Fe0.2O3− (Ln=La, Pr, Nd, Sm, Gd) for the electrode in solid oxide fuel cells, *Solid State Ionics*, 1999, **117**, 277–281.

99 M. Keane, M. K. Mahapatra, A. Verma and P. Singh, LSM–YSZ interactions and anode delamination in solid oxide electrolysis cells, *Int. J. Hydrogen Energy*, 2012, **37**, 16776–16785.

100 P. Hjalmarsson, X. Sun, Y.-L. Liu and M. Chen, Durability of high performance Ni–yttria stabilized zirconia supported solid oxide electrolysis cells at high current density, *J. Power Sources*, 2014, **262**, 316–322.

101 S. J. Kim and G. M. Choi, Stability of LSCF electrode with GDC interlayer in YSZ-based solid oxide electrolysis cell, *Solid State Ionics*, 2014, **262**, 303–306.

102 Z. Pan, Q. Liu, M. Ni, R. Lyu, P. Li and S. H. Chan, Activation and failure mechanism of La0.6Sr0.4Co0.2Fe0.8O3−δ air electrode in solid oxide electrolyzer cells under high-

current electrolysis, *Int. J. Hydrogen Energy*, 2018, **43**, 5437–5450.

103 Q. Fang, L. Blum and N. H. Menzler, Performance and Degradation of Solid Oxide Electrolysis Cells in Stack, *J. Electrochem. Soc.*, 2015, **162**, F907–F912.

104 P. Hjalmarsson, M. Søgaard and M. Mogensen, Electrochemical performance and degradation of (La0.6Sr0.4)0.99CoO3−δ as porous SOFC-cathode, *Solid State Ionics*, 2008, **179**, 1422–1426.

105 H. Wang, K. J. Yakal-Kremski, T. Yeh, G. M. Rupp, A. Limbeck, J. Fleig and S. A. Barnett, Mechanisms of Performance Degradation of (La,Sr)(Co,Fe)O 3-δ Solid Oxide Fuel Cell Cathodes, *J. Electrochem. Soc.*, 2016, **163**, F581–F585.

106 E. Lay-Grindler, J. Laurencin, J. Villanova, I. Kieffer, F. Usseglio-Viretta, T. Le Bihan, P. Bleuet, A. Mansuy and G. Delette, Degradation Study of the La 0.6 Sr 0.4 Co 0.2 Fe 0.8 O 3 Solid Oxide Electrolysis Cell (SOEC) Anode after High Temperature Electrolysis Operation, *ECS Trans.*, 2013, **57**, 3177–3187.

107 K. Chen and S. P. Jiang, Surface Segregation in Solid Oxide Cell Oxygen Electrodes: Phenomena, Mitigation Strategies and Electrochemical Properties, *Electrochem. Energy Rev.*, 2020, **3**, 730–765.

108 G. Rinaldi, A. Nakajo, M. Hubert, D. F. Sanchez, J. Laurencin, P. Burdet and J. van Herle, ed. *Proc. 13th Symposium on Modeling & Validation of Fuel Cells*, ausanne, Switzer-land, 2016.

109 T. Matsui, M. Komoto, H. Muroyama, K. Kishida, H. Inui and K. Eguchi, Degradation factors in (La,Sr)(Co,Fe)O3-cathode/Sm2O3–CeO2 interlayer/Y2O3–ZrO2 electrolyte system during operation of solid oxide fuel cells, *J. Power Sources*, 2016, **312**, 80–85.